Electric and magnetic variations in the near-Mars environment

C. M. Fowler, L. Andersson, J. Halekas, J. R. Espley, C. Mazelle, E. R. Coughlin, R. E. Ergun, D. J. Andrews, J. E. P. Connerney, B. Jakosky

To cite this version:

C. M. Fowler, L. Andersson, J. Halekas, J. R. Espley, C. Mazelle, et al.. Electric and magnetic variations in the near-Mars environment. Journal of Geophysical Research Space Physics, 2017, 122, pp.8536-8559. ⟨10.1002/2016JA023411⟩. ⟨insu-03676960⟩

AGU PUBLICATIONS

JGR

Journal of Geophysical Research: Space Physics

RESEARCH ARTICLE
10.1002/2016JA023411

Special Section:
Major Results From the MAVEN Mission to Mars

Key Points:
- First statistical study of the distribution of electric field wave power in the Martian magnetosphere
- Wave power from magnetosheath is observed to reach the upper ionosphere in all of 140 cases in a smaller statistical study
- Solar wind IMF orientation shown to significantly affect the statistical distribution of wave power in the Martian magnetosphere

Correspondence to:
C. M. Fowler,
christopher.fowler@lasp.colorado.edu

Citation:
Fowler, C. M., L. Andersson, J. Halekas, J. R. Espley, C. Mazelle, E. R. Coughlin, R. E. Ergun, D. J. Andrews, J. E. P. Connerney, and B. Jakosky (2017), Electric and magnetic variations in the near-Mars environment, *J. Geophys. Res. Space Physics*, *122*, 8536–8559, doi:10.1002/2016JA023411.

Received 30 AUG 2016
Accepted 27 JUL 2017
Accepted article online 9 AUG 2017
Published online 29 AUG 2017

Electric and magnetic variations in the near-Mars environment

C. M. Fowler[1], **L. Andersson**[1], **J. Halekas**[2], **J. R. Espley**[3], **C. Mazelle**[4], **E. R. Coughlin**[5,6], **R. E. Ergun**[1], **D. J. Andrews**[7], **J. E. P. Connerney**[3], **and B. Jakosky**[1]

[1]Laboratory for Atmospheric and Space Physics, University of Colorado Boulder, Boulder, Colorado, USA, [2]Department of Physics And Astronomy, University Of Iowa, Iowa City, Iowa, USA, [3]NASA Goddard Space Flight Center, Greenbelt, Maryland, USA, [4]IRAP, University of Toulouse, CNRS, UPS, CNES, Toulouse, France, [5]Astronomy Department and Theoretical Astrophysics Center, University of California, Berkeley, California, USA, [6]Einstein Fellow, [7]Swedish Institute for Space physics, Uppsala, Sweden

Abstract For the first time at Mars the statistical distribution of (1-D) electric field wave power in the magnetosphere is presented, along with the distribution of magnetic field wave power, as observed by the Mars Atmosphere and Volatile EvolutioN spacecraft from the first 14.5 months of the mission. Wave power in several different frequency bands was investigated, and the strongest wave powers were observed at the lowest frequencies. The presented statistical studies suggest that the full thermalization of ions within the magnetosheath does not appear to occur, as has been predicted by previous studies. Manual inspection of 140 periapsis passes on the dayside shows that Poynting fluxes (at 2–16 Hz) between $\sim 10^{-11}$ and 10^{-8} Wm^{-2} reach the upper ionosphere for all 140 cases. Wave power is not observed in the ionosphere for integrated electron densities greater than $10^{10.8}$ cm^{-2}, corresponding to typical depths of 100–200 km. The observations presented support previous suggestions that energy from the Mars-solar wind interaction can propagate into the upper ionosphere and may provide an ionospheric heating source. Upstream of the shock, the orientation of the solar wind interplanetary magnetic field was shown to significantly affect the statistical distribution of wave power, based on whether the spacecraft was likely magnetically connected to the shock or not—something that is predicted but has not been quantitatively shown at Mars before. In flight performance and caveats of the Langmuir Probe and Waves electric field power spectra are also discussed.

1. Introduction

The lack of a significant intrinsic magnetic field at Mars and the subsequent interaction of the solar wind with the Martian ionosphere [*Acuna et al.*, 1998] leads to an induced magnetosphere at the planet [e.g., *Bertucci et al.*, 2011]. The Martian bow shock typically lies at a planetocentric distance of ∼1.6 Martian radii [e.g., *Slavin et al.*, 1991; *Vignes et al.*, 2000; *Trotignon et al.*, 2006]—much closer than, for example, the typical terrestrial bow shock location that lies at ∼14.6 Earth radii [e.g., *Fairfield*, 1971] as a result of the Earth's large intrinsic dipole magnetic field. The much smaller scale of the magnetosphere and lack of a global dipole field, for unmagnetized bodies, lead to different physical mechanisms dispersing the upstream solar wind kinetic energy and subsequent facilitation of energy transfer from the solar wind down to the upper atmosphere and ionosphere of the planet [e.g., *Mazelle et al.*, 2004]. Plasma waves within the magnetosphere are one such energy transfer mechanism.

The first measurements of plasma waves at Mars were made by the Phobos 2 spacecraft [*Grard et al.*, 1989]; the Plasma Wave System observed several plasma boundaries and regions including the bow shock, magnetosheath, and a boundary termed the "planetopause" (defined as a magnetic enhancement separating shocked solar wind plasma from the colder, heavier planetary plasma). These boundaries and regions were observed to vary in position over multiple orbits. Within the so-called planetopause, the Plasma Wave System identified bursts of waves interpreted as whistler wave modes. The planetopause has since been confirmed to be the same boundary as the more commonly known magnetic pileup boundary (MPB) [*Trotignon et al.*, 1996, 2006].

Wave activity in the region of the bow shock was reported by *Sagdeev et al.* [1990]. They proposed that high-frequency waves excited at the shock front were due to currents flowing along this front which were subsequently convected downstream to inside of the magnetosheath by the solar wind. Cold Martian ionospheric ions diffusing through the planetopause to the magnetosheath were thought to generate lower-frequency waves observed close to the bow shock.

Waves at the local proton cyclotron frequency have been observed upstream of Mars by several studies. To our knowledge, *Russell et al.* [1990] were the first to report these observations, suggesting that the cause of these waves was the pickup of newly formed protons from the ionization of the Martian hydrogen corona. The waves reported by *Russell et al.* [1990] were rare in occurrence, lasting only for short durations (tens of minutes) and consisted of relatively low amplitude (~0.15 nT) waves in the magnetic field observations. Observations of waves at the local proton cyclotron frequency upstream of Mars were observed by the Mars Global Surveyor (MGS) mission for much longer durations of time and at larger wave amplitudes [*Brain et al.*, 2002]. *Bertucci et al.* [2013] found correlations between the occurrence of waves upstream at the local proton cyclotron frequency measured by the MGS spacecraft and modeled densities of the hydrogen corona at Mars, further supporting the proposition that ionization of the Martian hydrogen corona drives upstream proton cyclotron waves. More recently, *Romanelli et al.* [2016] have reached the same conclusion using Mars Atmosphere and Volatile EvolutioN (MAVEN) data with a similar, but more elaborate, data analysis methodology that used an up-to-date model for the hydrogen exospheric densities. Indeed, it is now commonly accepted that the ionization of the neutral Martian corona upstream of the shock (that consists primarily of H), and the subsequent ion-ion resonant instabilities that arise between the newly ionized protons and flowing solar wind, leads to the generation of waves observed at almost the local proton cyclotron frequency [e.g., *Gary*, 1991; *Delva et al.*, 2011]. The relative motion between the spacecraft and the solar wind causes a Doppler shift within the spacecraft frame of measurement, and thus, these waves may appear at frequencies close to, but not exactly at, the local proton cyclotron frequency in the spacecraft frame. The most efficient wave generation occurs if ion gyration is resonant with a wave in the plasma—the gyrating ion subsequently sees a constant electric field and can quickly gain significant energy [*Delva et al.*, 2011].

Empirical locations of the Martian bow shock have been calculated based on observations by the Mariner 4, MARS 2, MARS 3, MARS 5, and Phobos 2 spacecraft [*Slavin et al.*, 1991]. The altitude of the Martian bow shock was not observed to vary with solar cycle, in contrast to what is observed at Venus. This was attributed to Venus's weak but significant intrinsic magnetic field. Similar analysis has been carried out by other authors [e.g., *Vignes et al.*, 2000; *Trotignon et al.*, 2006] who used data from the Phobos 2 and MGS missions to improve the previous empirical location models of the bow shock and MPB.

Low-frequency (LF) waves have been observed at Mars by various authors analyzing magnetic field data from the MGS spacecraft. *Brain et al.* [2002] observed waves upstream of the bow shock close to the local proton cyclotron frequency whose amplitudes (occurrence) tended to decrease (increase) with increasing distance from the bow shock. They also observed whistler waves propagating upstream of the bow shock when MGS was magnetically connected to the shock front. *Bertucci et al.* [2004] observed LF waves on either side of the MPB. Waves upstream of the MPB were found to be mirror mode waves, while those downstream were large-amplitude fast magnetosonic waves. *Espley et al.* [2004] observed LF compressional waves in the dayside sheath with frequencies many times less than the local proton frequency. These LF waves were much more varied in type on the nightside and were typically transverse to the field with frequencies closer to the local proton cyclotron frequency.

More recently, LF waves upstream of Mars observed by MAVEN were analyzed by *Ruhunusiri et al.* [2015]. They found that Alfvén waves were dominant upstream and in the magnetosheath, with fast waves observed frequently near the bow shock and MPB. The occurrences of these Alfvén and fast waves varied with upstream solar wind dynamic pressure.

The relatively short mission lifetimes of the early Mariner, MARS, and Phobos missions, the lack of a plasma wave instrument or magnetometer on the Mars EXpress (MEX) spacecraft, and the Sun synchronous orbit of MGS mean that previous observations of waves and plasma boundaries within the Martian magnetosphere have been limited in number, spatial, and temporal coverage. MAVEN is the first spacecraft to visit Mars carrying both a magnetometer and electric field instrument and to be in an orbit such that the entire magnetosphere will eventually be sampled.

The goal of this paper is to provide an overview of the MAVEN electric and magnetic data sets and to discuss these data sets (that span several plasma regions and boundaries) in light of the previous literature. We thus present here statistical maps of the magnetic and electric field wave power, taken over the first ~14.5 months of the MAVEN mission, throughout the Martian magnetosphere. The remainder of this paper is as follows: the data used in this analysis are described in section 2, including caveats of the Langmuir Probe and Waves (LPW) electric field power spectral data set. Section 3 outlines the analysis method. Statistical maps of electric and magnetic field wave power are presented in section 4. Results are presented from a smaller statistical study demonstrating that wave power (assumed to propagate downward from the sheath) reaches the upper ionosphere of Mars. A third statistical study demonstrates that the distribution of wave power within the Martian magnetosphere is strongly influenced by the upstream solar wind interplanetary magnetic field (IMF) orientation, something that has been predicted but never before presented in a statistical study of in situ data at Mars. A discussion of these results follows in section 5 before conclusions are presented in section 6.

2. Data

The MAVEN spacecraft reached Mars in September 2014 and achieved its final science orbit shortly thereafter [*Jakosky et al.*, 2015]. Periapsis is typically at 150 km and apoapsis reaches approximately 6500 km in altitude. The elliptical nature of the orbit and subsequent precession about the planet means that MAVEN is able to sample the solar wind on a regular basis, obtaining upstream conditions that drive the downstream magnetosphere and ionosphere. Of interest to this study are data from the Langmuir Probe and Waves (LPW) [*Andersson et al.*, 2015], Magnetometer (MAG) [*Connerney et al.*, 2015], and Solar Wind Ion Analyzer (SWIA) [*Halekas et al.*, 2015] instruments.

LPW consists of two ~7 m booms separated by an angular distance of ~110°. The instrument alternates between operating as a Langmuir probe measuring current voltage (I–V) characteristics and operating as an electric field instrument measuring waves. The designed operation cycle consists of four subcycles that are performed the same way regardless of measurement cadence. The four subcycles for the nominal mission are as follows: I–V measurement on boom 1, “passive” (PAS) wave measurement, I–V measurement on boom 2, and “active” (ACT) wave measurement. The difference between the PAS and ACT wave measurements is that prior to the ACT measurement a weak white noise broadcast (sounding) is performed, designed to stimulate waves at the local plasma frequency. Section 2.1 outlines in more detail these differences. Electric field power spectra (and I–V characteristics) are measured at cadences between 2 and 128 s depending on the instrument mode of operation. MAG is a fluxgate magnetometer that measures the vector magnetic field at a rate of 32 Hz. SWIA is an electrostatic top hat analyzer that measures ion fluxes from 25 eV up to 25 keV with a field of view spanning 360° × 90°. The upstream solar wind parameters used in this study were derived from SWIA using moments that are calculated onboard, at a cadence of 4 s. A detailed description of this method is given in *Halekas et al.* [2016].

LPW electric field wave spectra are available for the first ~14.5 months of the MAVEN mission, from 10 October 2014 to 9 December 2015. Due to a change in instrument operation, wave spectra are not available on a regular basis after these dates. The bulk of the Martian ionosphere is typically observed below 600 km, and as such only data above 600 km were analyzed in the statistical studies outlined in sections 3.1 and 3.3 of this study. Taking into account this altitude range, the LPW data set consists of 3,308,714 spectra (1,415,620 active and 1,893,094 passive). MAVEN orbit coverage was such that the spacecraft sampled the upstream solar wind for approximately 8.5 months of this data set, between roughly December 2014 to mid-March 2015 and June to November 2015. Analysis utilizing upstream solar wind drivers is subsequently limited to these time ranges, resulting in a total of 2,051,270 spectra (920,612 active and 1,130,658 passive) available for analysis. Before detailing the specifics of our analysis we first discuss the general properties of the LPW wave spectra and outline important caveats when analyzing this data set. A discussion of the caveats of the LPW I–V characteristics is currently under preparation, for submission to his journal.

2.1. Description and Caveats of the LPW Wave Spectra Data Set

The LPW electric field wave spectra are produced by measuring the potential difference as a time series between the two LPW booms, the ends of which are separated by a distance of 12.68 m. The instrument measures the electric field the same way in both the PAS and the ACT subcycles. Both subcycles produce a low time resolution, 64 point-per-subcycle electric field DC time series data product that is sent to ground. The full resolution time series data are analyzed via an on board fast Fourier transform (FFT) which is applied to three different frequency ranges: low (LF_{lpw}, 0.25 Hz–496 Hz), medium (MF_{lpw}, 16 Hz–3.2×10^4 Hz), and high (HF_{lpw}, 1 kHz–2 MHz) frequencies. The subscript lpw denotes that these ranges apply to the LPW level 2 spectra

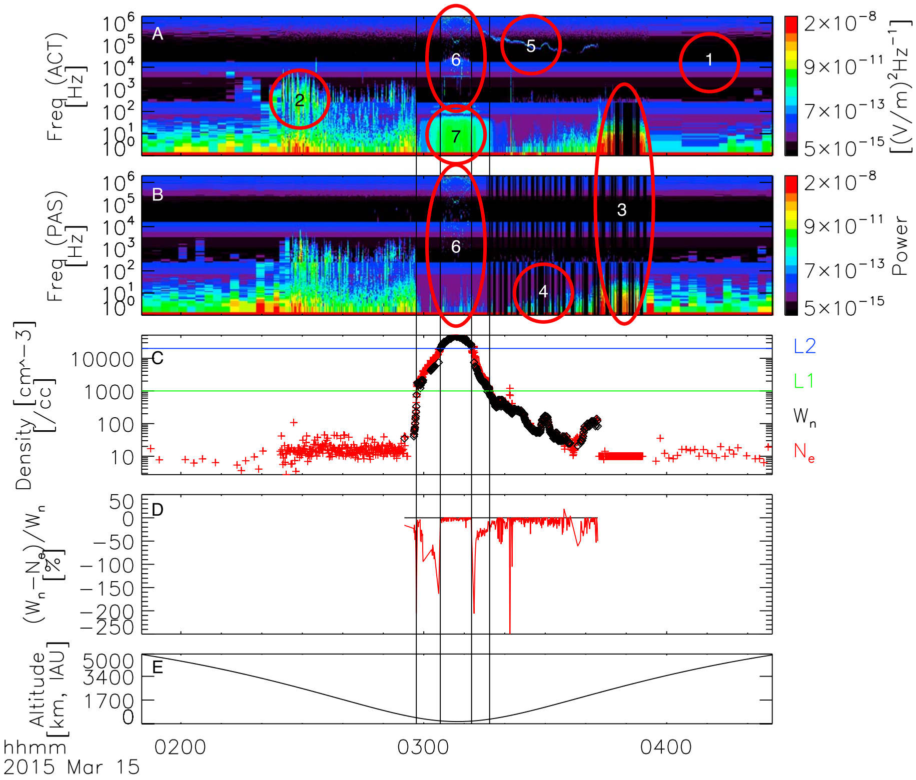

Figure 1. Highlighted caveats of the LPW wave spectra that are discussed in the text. (a and b) The ACT and PAS wave spectra. (c) The local electron density derived from the LPW wave sounding measurements in black and the Langmuir probe in red. (d) The percentage difference between these quantities. (e) The spacecraft altitude. The lines L1 and L2 mark densities of 1×10^3 cm^{-3}a and 2×10^4 cm^{-3}, respectively. The four vertical black lines mark where the Langmuir probe-derived densities in Figure 1c cross these values.

as opposed to the frequency ranges used for the study presented in section 3 of this paper. The resulting power spectra (known as survey data) are sent to ground, but the high-resolution time series data for the three frequency ranges are not sent to ground on a regular basis due to telemetry restrictions. This high-resolution time series data can be sent to ground via a burst system. When activated, the burst system selects the highest amplitude data from a fixed length time window. Subsequently, burst data sent to ground span small periods of time. Burst data are only available during the PAS subcycle. As mentioned, the main difference between the PAS and ACT subcycles is that for the ACT subcycle, low power white noise is broadcast just prior to capturing the electric field measurement. This white noise is broadcast to increase the probability of measuring the Langmuir (plasma) line and thereby obtain an absolute plasma density measurement. Typically, multiple FFTs from the same subcycle are averaged during onboard processing when capturing the PAS $\mathrm{MF_{lpw}}$ and $\mathrm{HF_{lpw}}$ spectra, and the number of FFTs averaged can be changed. For the ACT subcycle only the first FFT after the white noise broadcast is recorded. This difference between ACT and PAS onboard processing can lead to slight differences between spectra captured at neighboring points in time. This is particularly true at high altitudes when the cadence of level 2 spectra can be up to 128 s. An example can be seen just to the left of circle 2 in Figures 1a and 1b at approximately 10^3 Hz.

Example wave spectra are shown in Figure 1. LPW wave spectra from ACT and PAS subcycles are shown in Figures 1a and 1b, respectively. Figure 1c shows the local electron density as determined by the local plasma line from the electric field waves measurement in black and the Langmuir probe-derived density in red; Figure 1d shows the percentage difference between these two quantities. "W_n" stands for waves-derived electron density; "N_e" stands for Langmuir probe-derived density in this panel. The green and blue horizontal lines in Figure 1c mark densities of 1×10^3 and 2.3×10^4 cm^{-3} (the importance of which is discussed in section 2.1.3). The vertical black lines mark where the Langmuir probe-derived densities cross these values. Figure 1e shows the spacecraft altitude in the International Astronomical Union Mars planetocentric (IAU-Mars) frame. The ACT and PAS spectra both span a frequency range of just below 1 Hz up to ~2 MHz but are composed of three separate, merged spectra spanning smaller-frequency ranges.

2.1.1. Combining the LF_{lpw}, MF_{lpw}, and HF_{lpw} Spectral Ranges

The noise floor for each of the three individual frequency bands (LF_{lpw}, MF_{lpw}, and HF_{lpw}) is frequency dependent. These three bands are combined to produce the level 2 data products shown in Figures 1a and 1b. This noise floor is present in the form of three horizontal bands at constant frequency, close to ~500 Hz, ~2000 Hz, and ~2 MHz in the final level 2 product, and an example of this discontinuity is highlighted by circle 1 in Figure 1. The three individual frequency bands partially overlap in frequency space, and the frequency bin sizes at these regions of overlap are different in size due to the quasi-logarithmic scaling used in frequency space. As such, no further processing is carried out when the LF_{lpw}, MF_{lpw}, and HF_{lpw} spectra are combined; they are simply "cut" and joined at empirically determined frequencies to produce the continuous spectrum in the level 2 data products shown in Figure 1. When electric field waves are present the three separate frequency bands are well (but not perfectly) calibrated, as shown by circle 2 in Figure 1, where there is no significant change in wave power across the two frequency bands at ~500 Hz.

2.1.2. Flagging Low-Quality Spectra

Spectra of low-quality have been removed resulting in "empty" blocks within the final level 2 spectra. Examples are highlighted by circles 3 and 4 in Figure 1, here shown by black blocks in the spectra. The degradation of spectra can arise for several reasons, and we discuss the most important here. The primary source of spectra degradation arises from instrument-induced DC electric fields. When wave spectra are captured, the instrument operates as a "reverse Langmuir probe." Rather than applying a voltage to one of the probes and measuring the resultant current collected by that probe, a current is applied to both probes and the resultant voltages on each measured. There is an optimum range of "bias" currents that should be applied to each probe, whereby voltage is approximately proportional to the natural log of current, and there is a corresponding unique voltage value that can be observed. This region is known as the "ramp" or "electron temperature fit" region on a Langmuir probe I–V curve [see, e.g., *Ergun et al.*, 2015]. If the applied bias current lies outside of this optimum range, then voltage is almost constant with respect to current, and there are many nonunique voltage values that can accompany this bias current value. Due to differences in the LPW probe surface characteristics, these optimum bias currents are slightly different for each probe. If one, or both, of these applied bias currents lies outside of their optimum ranges, the corresponding measured voltages for both probes can swing to large values, typically inducing large instrumental DC electric fields that swamp any real ambient electric fields. The low-density plasma environment at Mars makes this optimum bias current region narrower than on previously flown Langmuir probes at Earth, for example. The highly variable nature of the Martian plasma environment throughout a MAVEN orbit further increases the difficultly in applying the optimum bias currents at all times during one orbit. Subsequently, the blank spectra marked by circles 3 and 4 in Figure 1 can be common, particularly during the early mission when calibration was ongoing. These large instrumental DC electric fields can be identified within the LPW ancillary data and are used to identify and flag these low-quality spectral measurements.

Minor attitude control thruster firings typically occur on the outbound segment of each orbit. These events are recorded within MAVEN ancillary engineering data files which are used to identify thruster firing events within the LPW wave spectra. Contamination of the LPW waves data from these firings is much less frequent than contamination due to instrument induced DC fields.

LPW does not record wave spectra when capturing high cadence burst data, but this happens less frequently than the inducement of instrumental DC electric fields and attitude control thruster firings. The lowest measured frequency bin for the LPW wave spectra usually contains noise and is typically not useful: the usable frequency range is subsequently quoted as upward of 2 Hz. Additional noise can also be present below ~100 Hz as is discussed in section 2.1.5.

2.1.3. Wave Sounding

The operation and onboard processing of the ACT and PAS measurements are identical with the difference of the weak white noise broadcast prior to the ACT measurements. PAS spectra are typically an average of multiple FFTs; ACT spectra consist of the single FFT processed immediately after a wave sounding. As stated above this sounding is an attempt to excite the local plasma line, allowing the local density to be derived with high accuracy. The instrument upper frequency range of 2 MHz limits the measurable upper density range to below about 2.3×10^4 cm^{-3}. Circle 5 in Figure 1 demonstrates the plasma line observed in the ACT spectra. When comparing ACT and PAS spectra, it is clear that the sounding is a success and is an important instrument capability. A review of the first wave sounding density measurements observed by LPW and MAVEN is presented by *Andrews et al.* [2015], who observed influences from local crustal magnetic fields that are consistent with previous observations at Mars. For the MAVEN mission the density values derived from the waves measurements are held as the "gold standard" for all plasma density measuring instruments.

The LPW instrument unintentionally amplifies measured electric field signals for waves that have wavelengths close to the sensor size. This translates to amplified wave power at high frequencies and is only an issue at densities above $\sim 1 \times 10^4$ cm^{-3} when the corresponding plasma frequency is high. The derived plasma density is a function of frequency and not signal amplitude. Somewhat fortunately, this allows for an accurate determination of the local plasma line: the enhancement in measured power typically makes it easier to determine the local plasma line in the wave spectra. This effect occurs for the PAS and ACT subcycles, resulting in amplified wave power at densities close to and above $\sim 1 \times 10^4$ cm^{-3}. The effect is similar to that observed on the Polar satellite [*Kolesnikova et al.*, 2001; *Kolesnikova and Beghin*, 2001]. Within the instrument the signal amplitude grows to the instrument limit, and distortion/clipping of the signal occurs. This results in aliasing or "ghost peaks" in the derived FFT wave spectra throughout the full frequency range of the instrument all the way into the LF range. Examples are highlighted in Figures 1a and 1b by circle 6; note the corresponding large electron densities in Figure 1c. The dominant wave power during these events remains in the local plasma line and so the local electron density can still be derived to high accuracy.

For densities greater than $\sim 2.3 \times 10^4$ cm^{-3}, the plasma line lies above the instrument frequency range. The effect of signal amplification still occurs, and aliasing and ghost peaks are still present in the derived FFT wave spectra despite the absence of the real local plasma line. Such high densities are typically only encountered close to the subsolar point at low altitudes and can be identified based on spacecraft position. If the corresponding LP-derived electron density is available, this can be used as a further proxy to identify times when the density approaches $\sim 2.3 \times 10^4$ cm^{-3}. During these time periods, when density approaches or is greater than $\sim 2.3 \times 10^4$ cm^{-3}, the waves derived density should not be used as the density lies outside of the instrument measurement range.

2.1.4. Effects of the Spacecraft Wake

The LPW instrument is one of the first Langmuir probes to demonstrate an effect produced by the spacecraft wake as a result of the large dynamic range of different plasma conditions encountered by the MAVEN spacecraft. Langmuir waves have been observed to exist in density cavities [e.g., *Ergun et al.*, 2008; *Malaspina*, 2010]. The sounding feature of the LPW instrument is designed to excite Langmuir waves, and circle 5 in Figure 1 demonstrates this. As the Debye length of the local ambient plasma shortens, it approaches the characteristic size of the spacecraft and spacecraft wake. The density in the spacecraft wake is a factor of ~2 lower than the ambient plasma, and as a result of the sounding, Langmuir waves accumulate in the spacecraft wake cavity and have much larger power than the non trapped waves in the ambient plasma. In Figure 1c the density measured by the LP is compared to that derived from the waves measurements. Below densities of $\sim 1 \times 10^3$ cm^{-3} and upward of 2×10^4 cm^{-3}, the two methods agree very well, within ~25%. Between the horizontal lines L1 and L2, the density derived from the waves measurements is lower by a factor of up to ~2. This effect may exist on other missions, but there are key aspects that have allowed the MAVEN mission to identify this: (1) the spacecraft is flying through a plasma where the Debye length is comparable to the spacecraft size, (2) multiple instruments measure the plasma density allowing density gradients to be compared, and perhaps most importantly, (3) due to the signal amplification discussed above, the LPW instrument measures the true density at small Debye lengths. Clear evidence of spacecraft wake effects can be seen from the anomalous density jump before and after crossing line L2 in Figure 1c. None of the other plasma density measuring instruments on the spacecraft observe such a density jump, indicating that the Langmuir waves before and after this jump have two different sources with a density difference of ~2. This is explained by the Langmuir waves that are observed between lines L1 and L2 originating from within the spacecraft wake. There are times when the Langmuir waves originating from the spacecraft wake and ambient plasma appear to coexist. Most importantly, the waves-derived density provides a baseline for the minimum ambient plasma density. Between $\sim 1 \times 10^3$ and 2×10^4 cm^{-3}, the waves-derived densities may be up to a factor of ~2 lower than the true ambient plasma density.

2.1.5. Low-Frequency Noise

The LPW subcycle prior to the waves measurement ends with setting the probe that has just performed an I–V sweep to the spacecraft potential. When the waves measurement starts, the potential on this sensor then floats to the ambient plasma potential and this coupling between the sensor and ambient plasma to achieve equilibrium takes time. The onboard FFT neglects the first two data measurements to account for this “equilibrium settling time.” However, under certain plasma conditions this settling time is longer than expected and as a result a DC signal is present at the start of the electric field time series measurement. When present, the onboard FFT of this DC signal produces a significant, low-frequency signal in the power spectrum. Ground data processing blocks out some such times (as seen by circle three in Figure 1), but the filter is set modestly such that if single LF spectra are removed, neighboring spectra should be treated with caution. Plasma conditions in the central Martian magnetotail often exhibit these conditions.

At high densities the ACT subcycle can contain low-frequency instrument noise which has been confirmed within the LF time series data. The signature within the onboard FFT can manifest itself as near constant power present below frequencies of ∼100 Hz. This noise varies in strength; an example is highlighted by circle 7 in Figure 1a. This noise can be identified when comparing ACT and PAS wave spectra.

The cadence between the individual wave spectra in the level 2 data product depends on the operation mode of the LPW instrument, which varies as a function of MAVEN’s altitude. Typically, higher-resolution data are available at periapsis, at a cadence of 2 s. At higher altitudes the resolution in time becomes coarser (due to telemetry restrictions and subsequent changes in instrument mode) and spectra are typically available every ∼128 s above 2000–3000 km, depending on the exact instrument mode being run at the time.

2.2. Example Spectra

An example of the electric and magnetic field power spectra for one MAVEN orbit at Mars is shown in Figure 2. Figures 2a and 2c show the ACT and PAS electric field power spectra, respectively. Figures 2b and 2d show the corresponding low time resolution electric field time series data for the ACT and PAS power spectra. The DC component has not been removed from Figures 2b and 2d. Figure 2e shows the magnetic field power spectrum, which has been derived using wavelet analysis of the 32 Hz time series magnetic field data. Lower resolution 1 Hz magnetic field time series data are shown in Figure 2f, which is clearer to interpret than the 32 Hz data, over a full MAVEN orbit. Figure 2g shows the spacecraft altitude in the IAU-Mars reference frame.

We note here an important detail with regard to the interpretation of electric and magnetic wave data and the inference of wave particle interactions, which was touched upon in section 1. Both pickup ions, and the MAVEN spacecraft, when located upstream of the Martian shock, can be assumed to be approximately at rest with respect to the planet. Waves-generated upstream as a result of ion-ion instabilities are thus detectable in the spacecraft frame at the local cyclotron frequency of the parent ion. Within the planetary magnetosphere (i.e., not in the solar wind), pickup ion conditions can be very different to the supersonic upstream case, and the association between waves detected by the spacecraft, and the local ion gyrofrequencies, may be less clear. Further, ULF waves have been observed to propagate through collisionless shock fronts, meaning that proton cyclotron waves-generated upstream of the shock can propagate into the sheath, where the magnetic field amplitude, and thus gyrofrequency, is different [e.g., *Shan et al.*, 2014]. In the remainder of this paper we make reference to the local ion gyrofrequencies at times when MAVEN is both upstream of the Martian shock and downstream of it within the magnetosphere. During all times we assume the simplest situation, i.e., that to first order, wave generation will occur at the local ion cyclotron frequency in the spacecraft frame. We note, however, that such an assumption may not be valid at all times.

The orbit is approximately in the dawn-dusk plane, spanning ∼4.5 h with periapsis occurring at just after 14:00 UTC. The inbound section is on the dawn, sunlit, southern hemisphere of Mars. Up until about 13:30 UTC MAVEN is in the solar wind, as visible by the relatively calm magnetic field in Figure 2f. The magnetic field strength is a few nanoteslas and shows little variation. This is mirrored in the magnetic field power spectrum in Figure 2g and the electric field power spectra in Figures 2a and 2c.

At around 13:30 UTC the electric and magnetic field data show disturbed features. The magnetic field power spectrum shows a brief increase in power of several orders of magnitude across the entire frequency range, before measuring strong wave power all the way through periapsis. This enhancement in wave power is the bow shock—the brief burst of wave power prior to the more continuous power measured may be due to the bow shock moving back across the spacecraft in response to changing upstream solar wind conditions or foreshock-related phenomena upstream of the shock itself. Based on the spacecraft position, orbit trajectory, and the shock location fits from *Vignes et al.* [2000], MAVEN crossed the bow shock at an oblique angle, ∼45°.

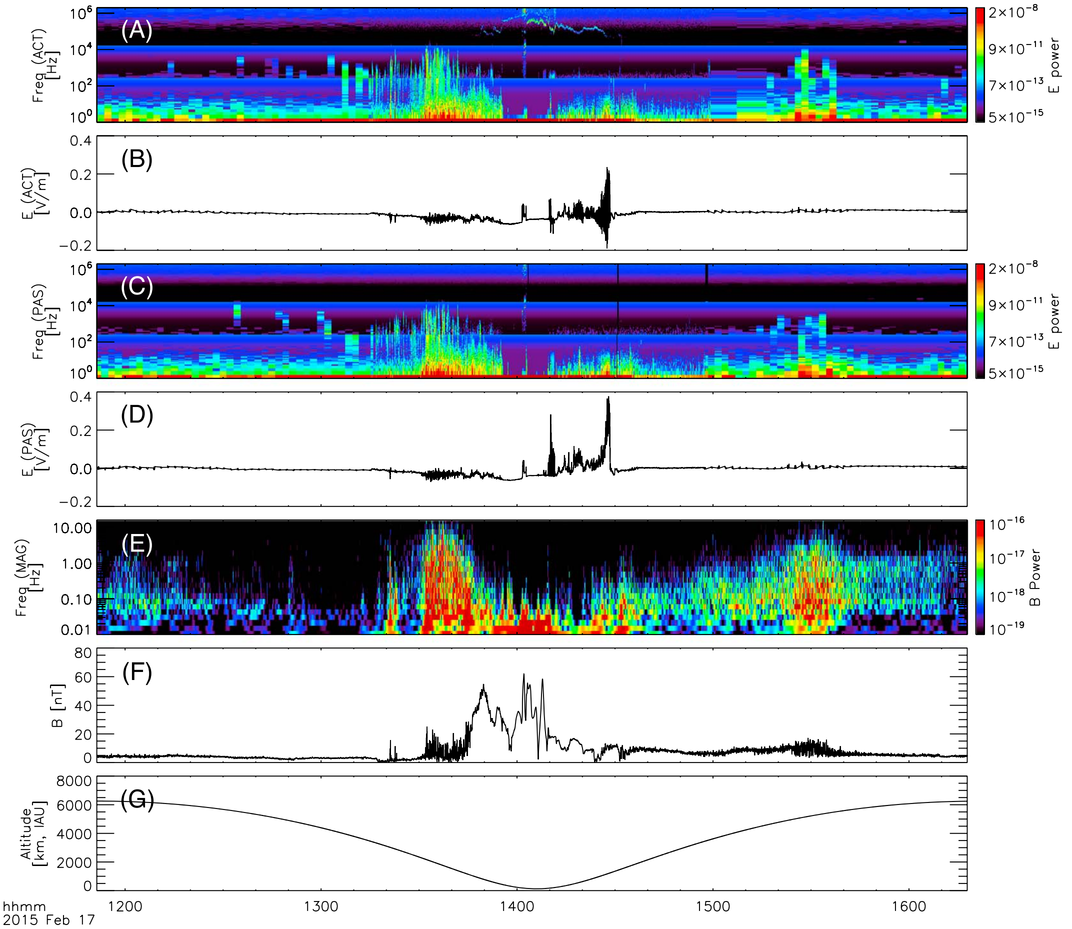

Figure 2. Example electric and magnetic field wave power spectra for one orbit about Mars. (a and c) The ACT and PAS electric field power spectra, respectively. (b and d) The time series electric field data from which these spectra were derived from. (e and f) The magnetic field power spectrum and the corresponding time series magnetic field data, respectively. (g) The spacecraft altitude in the IAU frame. *E* power has units of V^2 m^{-2} Hz^{-1}. *B* power has units of T^2 Hz^{-1}.

High-frequency electric and magnetic field wave power is observed by MAVEN as it crosses the bow shock. As the spacecraft approaches periapsis, wave power at higher frequencies drops off, as can be seen in Figures 2a, 2c, and and 2e. Periapsis occurs just past the dusk terminator in the northern hemisphere. There is very little electric field wave power observed in Figures 2a and 2c during periapsis but strong magnetic field wave power is observed at low frequencies below $\sim$0.1 Hz, seen in Figure 2e. The magnetic field strength is typically 20–40 nT throughout periapsis, resulting in local gyrofrequencies of heavier ions (O^+ and above) at and below this frequency range—on the order of <0.05 Hz. The large spacecraft velocity ($\sim$4 km s^{-1}) at periapsis means that it is not possible to tell whether these low-frequency waves are due to the gyromotion of heavy ions about the local magnetic field, or an artifact of the spacecraft traveling through the large-scale changing magnetic field topology. It is most likely a combination of the two—this study utilizes data above 600 km altitude where the effects of localized crustal magnetic fields and field-aligned currents (at times a large contributor to the large-scale magnetic field topology) are deemed negligible. Measurement uncertainty in the absolute magnetic field strength is less than 1 nT [*Connerney et al.*, 2015]. The upstream solar wind at Mars is typically $\sim$3 nT in strength and so a measurement uncertainty of <33% exists there. This study analyzes wave power within set frequency ranges (which are described in section 3.1), and such effects should be negligible here. For the worst-case example (i.e., the error in measured field strength is 1 nT), if the upstream solar wind has a field strength of 3 ± 1 nT, the corresponding local proton cyclotron frequency is 0.046 ± 0.015 Hz. This uncertainty lies mostly within one such frequency range analyzed in this study, 0.01–0.05 Hz. Within the shock and sheath, field strengths are typically at least 10 nT and the measurement uncertainty in magnetic field strength (<10%) is negligible for this study.

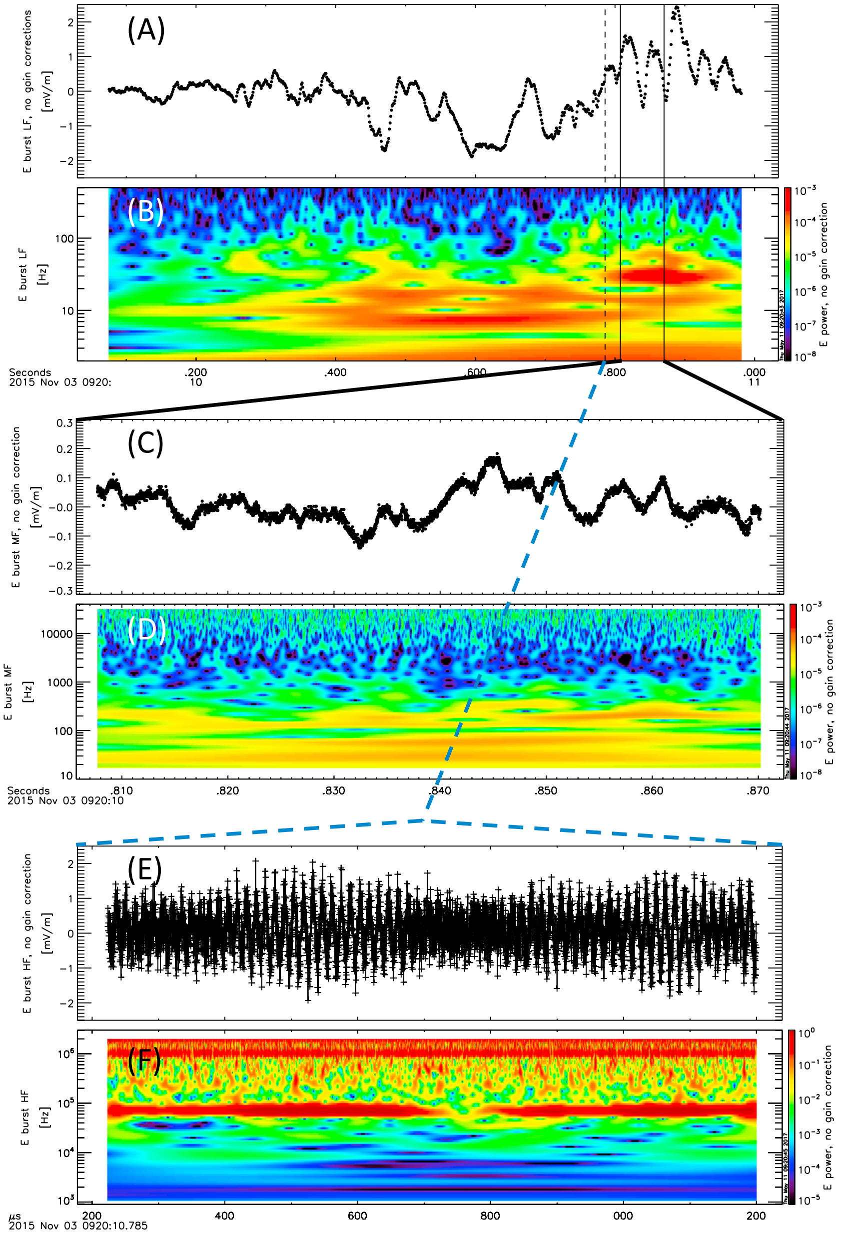

Figure 3. Example LPW electric field burst mode time series data. (a, c, and e) The LF_{lpw}, MF_{lpw}, and HF_{lpw} frequency ranges, respectively. (b, d, and f) Wavelet FFTs calculated on ground. Burst time series data are not gain corrected, and thus, signal amplitudes are not consistent across the three frequency ranges. *E* power has units of V^2 m^{-2} Hz^{-1}.

The outbound segment of the MAVEN trajectory passes across the nightside of the planet in the northern hemisphere, from dusk to dawn. Between ∼14:30 and 15:30 UTC MAVEN is in the magnetotail—the magnetic field power spectrum shows lower amplitude waves across a wide range of frequencies. The "bulge" in both electric and magnetic field wave power at roughly 15:30 UTC is most likely MAVEN exiting the magnetosheath and crossing the bow shock. Once MAVEN is back in the solar wind, the magnetic and electric field data in Figures 2a, 2c, and 2e quiet down. There is slightly more magnetic wave power after 15:30 UTC than before 13:00 UTC; analysis of the spacecraft orbit shows that the inbound part (before 13:00 UTC) sampled the upstream solar wind, while the outbound segment (after 15:30 UTC) sampled the downstream solar wind. The downstream solar wind is likely disturbed, causing these fluctuations. These fluctuations in Figure 2e are below 1 Hz and cannot be sampled by LPW, explaining why they are not present in Figures 2a and 2c.

There are several sporadic "blips" of electric field wave power observed at higher frequencies, between ∼10^2 and 10^3 Hz, observed with a slight preference at the bow shock and in the upstream solar wind. The measurement cadence of the MAG time series data prevents confirmation of the existence of these high-frequency bursts in the magnetic field data.

We note that several of the electric field wave spectra caveats discussed in section 2.1 are observed here; the stimulated plasma line at frequencies greater than ∼10^4 Hz at periapsis in Figure 2a, vertical black lines denoting flagged data in Figure 2c, and the three horizontal bands in Figures 2a and 2c marking the frequencies at which the LF_{lpw}, MF_{lpw}, and HF_{lpw} spectra have been merged into a single product.

2.2.1. Example Burst Mode Time Series Data

When operating in waves mode, the LPW instrument is capable of capturing short segments of higher time resolution, electric field time series data. These high cadence data are known as burst, or archive, data. The burst data capture is automatic, and the selection algorithm is described in *Andersson et al.* [2015]. The number of burst segments that can be sent to ground depends upon telemetry restrictions and thus varies throughout the MAVEN mission. Burst data are captured within the same three frequency bands as described above, namely, LF_{lpw}, MF_{lpw}, and HF_{lpw}. Burst data in the LF_{lpw} range consist of 1024 points measured over 1 s; burst data in the MF_{lpw} range consist of 4096 points measured over ∼0.0625 s. Burst data in the HF_{lpw} range consist of 4096 points measured over ∼0.000976 s.

The three burst frequency ranges do not always overlap in time. Example burst data from the three frequency ranges are shown in Figure 3, where for this example, the three frequency ranges do happen to overlap in time. The LPW level 2 time series data products are shown in Figures 3a, 3c, and 3e, for the LF_{lpw}, MF_{lpw}, and HF_{lpw} frequency ranges, respectively. Corresponding wavelet FFTs produced on the ground for these panels are shown in Figures 3b, 3d, and 3f. The burst time series data are not corrected for differences in frequency gain that are present between the three frequency ranges; thus, the amplitudes of the signals in Figures 3a, 3c, and 3e and the powers derived in the wavelet FFT spectra in Figures 3b, 3d, and 3f are not consistent. The LPW level 2 survey spectra (Figures 2a and 2c) are gain corrected on board the spacecraft.

The continuous signal observed at ∼1 MHz in Figure 3f is instrumental and its source is described in *Andersson et al.* [2015]. Closer inspection of the time series data shown in Figure 3e (not shown here due to space limitations) shows that approximately every other point is offset in amplitude, producing the observed signal at 1 MHz. The data points are joined by lines in Figure 3e to make the observed wave structure clearer to the reader.

The burst time series data can be subject to the caveats described in section 2.1, in particular, the low-frequency noise discussed in section 2.1.5. The examples shown in Figure 3 do not exhibit such noise; however, when present, it typically contaminates the first ∼100 measurement points of each burst.

3. Analysis Method

This study utilized data from the LPW, MAG, and SWIA instruments on board MAVEN. The LPW wave spectra are calculated on board the spacecraft via an FFT of high cadence electric field time series data. Magnetic field power spectra are obtained via a wavelet transform of the full resolution (32 Hz) magnetic field data on the ground. The LPW spectra are the most constrained in cadence and so magnetic field vector and power spectra measurements were paired to the LPW data set. The closest MAG data in time were paired to each LPW spectral measurement and were required to lie within 5 s of it. This pairing of data meant that the LPW and MAG data sets that are compared in this study consisted of even sample numbers. Given the much higher sampling rate of the MAG instrument (32 Hz), the magnetic field portion of this study could be carried out with significantly more data, although we note that the sheer volume of this data becomes problematic in terms of computational analysis time. MAG and SWIA data were used to calculate upstream solar wind parameters (which are discussed later) and the solar wind motional electric field direction. The upstream solar wind parameters were calculated as an average value for each orbit when MAVEN sampled the solar wind. These parameters were also paired to LPW and MAG spectral measurements and were required to lie within 6 h of these data. MAVEN's orbit is approximately 4.5 h long, and we assume that the solar wind does not change significantly over the course of one orbit. See *Halekas et al.* [2016] for more information on how upstream solar wind parameters are calculated from MAVEN data.

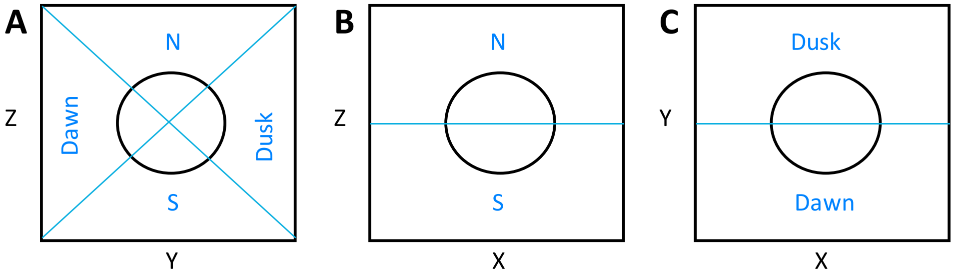

Figure 4. Cartoon diagram of the binning method used to produce statistical maps in this study. (a) The *Y-Z* plane cut into four regions—north (N), south (S), dawn, and dusk. (b and c) Data from these regions are used to produce the maps, looking at different planes. This system is used for both the MSO and MSE frames at Mars. Only data between $-1\ R_M < 1.5\ R_N$ are used when creating the statistical map shown in Figure 4a.

In-depth analysis of the physical processes acting within planetary shocks requires knowledge of the shock region being sampled by the spacecraft at the time of measurement, and, ideally, simultaneous observations of the upstream solar wind [e.g., *Bonifazi et al.*, 1980]. Several plasma boundaries and regions exist at Mars (for example, the foreshock, bow shock, magnetosheath, and MPB); descriptions of, and the detailed analysis required to identify, such boundaries have been well documented [e.g., *Gringauz*, 1976; *Rosenbauer et al.*, 1989; *Sagdeev et al.*, 1990; *Trotignon et al.*, 1996; *Acuna et al.*, 1998; *Mazelle et al.*, 2004]. Detailed analysis on such a large data set is outside the scope of this study, the goal of which is to provide an overview of the magnetic and electric variations at Mars and to show that such waves are incident on the upper ionosphere. Thus, we speculate on the regions that are likely observed in the following analysis but cannot confirm these speculations without more detailed analysis.

3.1. Electric and Magnetic Variations

The first part of this study analyzed power spectra of the 1-D electric field measurements from LPW and the magnetic field strength measured by MAG. Statistical maps were generated from the data set as a function of MAVEN position, in the Motional Solar wind Electric field (MSE), and Mars Solar Orbital (MSO) frames. The MSE frame is defined to point in the positive $\vec{E}$ direction, where $\vec{E} = -\vec{V}_{sw} x \vec{B}_{sw}$; $\vec{V}_{sw}$ and $\vec{B}_{sw}$ are the solar wind velocity and magnetic field vectors, respectively, in the MSO frame. In Cartesian coordinates, *X* points along the planet Sun direction, sunward pointing. *Z* points in the same direction as $\vec{E}$, and *Y* completes the right-handed system. Rotation from the MSO to MSE frame assumed that the solar wind velocity lay entirely in the radial direction outward from the Sun. Aberration due to Mars's orbital motion about the Sun was not taken into account, leading to an error in solar wind velocity direction of ~4°, which was negligible for this study. Statistical maps were compiled in the three planes: *X-Z*, *X-Y*, and *Y-Z*. Instead of simply compressing the third axis within each map, a more accurate binning method was used. The *Y-Z* map was split into four sections, based on dividers at 45° to the $Z = 0$ line. The boundaries were labeled north (N), south (S), dawn, and dusk, as shown in Figure 4a. Subsequent maps in the *X-Z* and *X-Y* planes utilized data only from the N and S, and dawn and dusk sections, respectively, as shown in Figures 4b and 4c. Data in the *Y-Z* map utilized data between $-1 < X < 1.5\ R_{mars}$.

Statistical maps were produced spanning several frequency ranges: ultralow frequency (ULF): 0.01–0.05 Hz; low frequency (LF): 1–5 Hz for magnetic field, and 2–5 Hz for electric field; medium frequency (MF): 5 Hz, high frequency (HF): 1 kHz–5 kHz. The MF range is the single frequency bin closest to 5 Hz in the power spectra; the ULF, LF, and HF ranges typically span ~4–5 frequency bins in the power spectra. The measurement cadence of MAG and LPW are such that wave spectra are available for both within the LF and MF ranges. Magnetic field spectra are available in the ULF range, and electric field spectra are available in the HF range. Justifications for these frequency ranges are discussed in section 3.4.

3.2. Wave Power Observed Within the Upper Ionosphere

The second part of this study analyzed 1 month of data from the dayside ionosphere to investigate whether wave power (assumed to originate from the sheath) was observed in the upper ionosphere. Such observations are predicted by *Moses et al.* [1988] and would support the theory that the shocked solar wind plasma does not have sufficient space to fully thermalize before encountering the planetary atmosphere and ionosphere of Mars, enabling direct energy transfer to these regions. A total of 140 inbound periapsis passes, spanning 2015-10-01 to 2015-10-30, was analyzed by hand.

The analysis included estimates of the Poynting flux using a method similar to, for example, *Hartinger et al.* [2013], which was adapted because the LPW instrument only measures one component of the electric field. The analysis was carried out within the frequency range 2–16 Hz, which is the range that the electric and magnetic field power spectra overlap. The different measurement cadences of the LPW and MAG instruments mean that the number, and widths, of frequency bins within the 2–16 Hz range, differ between the two spectra. Thus, each bin within the 2–16 Hz range was normalized (multiplied) by its width in frequency (Hz). Taking the square root of the subsequent normalized power yields values with units Vm^{-1} and T, for the electric and magnetic field, respectively. Thus, these values represent dE and dB, the amplitudes of the variations in the electric and magnetic field, respectively, as derived by the FFT and wavelet analysis. Because several frequency bins lie within the 2–16 Hz range, several values of dE and dB exist (one for each bin); the mean Poynting flux (in units of Wm^{-2}) was calculated using equation (1):

$$\mathrm{PF}_{\mathrm{mean}} = \frac{\mathrm{d}E_{\mathrm{mean}}\mathrm{d}B_{\mathrm{mean}}}{\mu_0}, \tag{1}$$

where $\mathrm{d}E_{\mathrm{mean}}$ and $\mathrm{d}B_{\mathrm{mean}}$ are the mean dE and dB values derived from a particular spectrum and μ_0 is $4\pi\times10^{-7}$ in MKS units. This method assumes that the 1-D electric field wave power is representative of the magnitude of electric field wave power and that the magnitude of electric and magnetic field wave powers are transverse and in phase such that an estimate of the Poynting flux can be obtained by multiplying dE and dB. These estimates are thus upper limits of Poynting flux present in the 2–16 Hz range. For the remainder of this paper, the term Poynting flux refers to the Poynting flux calculated within the 2–16 Hz range.

An example of one such periapsis from this analysis is shown in Figure 5. Figure 5a shows the electric field power spectrum between 2 and 100 Hz; Figure 5b shows the magnetic field power spectrum between 0.01 and 16 Hz (the white horizontal line marks 2 Hz, to compare with Figure 5a; the other two white lines show the local proton and O^+ gyrofrequencies); Figure 5c shows an estimate of the Poynting flux; Figure 5d shows the total electric field wave power summed between 2 and 100 Hz; and Figure 5e shows the ionospheric electron density, as derived from wave sounding by the LPW instrument. The spacecraft position within the MSO frame, and the spacecraft solar zenith angle (SZA), are marked across the bottom of the figure; the spacecraft travels southward with very little variation in the Y coordinate. The spacecraft samples the sheath close to the subsolar point and enters the ionosphere as it traverses into the southern hemisphere. Precession of the spacecraft over time is slow enough such that the 140 orbits analyzed here shared a similar geometry.

For the example shown in Figure 5, the spacecraft encounters the upper ionosphere just prior to 07:52 UTC, denoted by the left solid vertical line. At times earlier to this, the spacecraft is sampling the sheath, marked by the large electric and magnetic field wave powers. Wave power is observed well into the upper ionosphere, up until just before 07:58 UTC, marked by the right solid vertical line. The ionospheric density initially increases quickly up to a value of a few hundred cm^{-3} and increases more gradually after 07:53 UTC. Poynting flux and total electric field power (Figures 5c and 5d) show sharp reductions during the initial, sudden density increase, followed by more gradual reductions thereafter.

The vertical lines were identified manually; the upper ionosphere ("top boundary," left line) was defined as the point at which ionospheric densities were consistently greater than $\sim$20 cm^{-3}. The extent to which wave power was observed in the ionosphere ("E field boundary," right line) was defined as the point at which the total electric field power (Figure 5d) reached its background value of about 1.5×10^{-12} $(\mathrm{V/m})^2\mathrm{Hz}^{-1}$. Note that as in Figure 5a here, bursts of wave power are sometimes observed within the ionosphere; the right-hand line marked the extent to which wave power was continuously observed from the sheath. The dashed vertical line marks an example where a burst of wave power is coincident with a decrease in ionospheric density; such events occur frequently in the ionosphere but are not the subject of this paper.

The line profiles in Figures 5c and 5d are similar in shape, and this arises because there is very little magnetic wave power above 2 Hz within the ionosphere. Thus, the value of dB for the calculation of Poynting flux is essentially constant at the background level observed in Figure 5b, and dE is the primary varying component in this calculation. This is why the solid right-hand vertical line is marked based upon the total electric field value, rather than Poynting flux. We none-the-less show the estimated Poynting fluxes here because they provide an upper estimate of Poynting flux (in the 2–16 Hz range) at the top of the ionosphere, when magnetic variations are present above 2 Hz. This electrostatic-like behavior above 2 Hz within the ionosphere

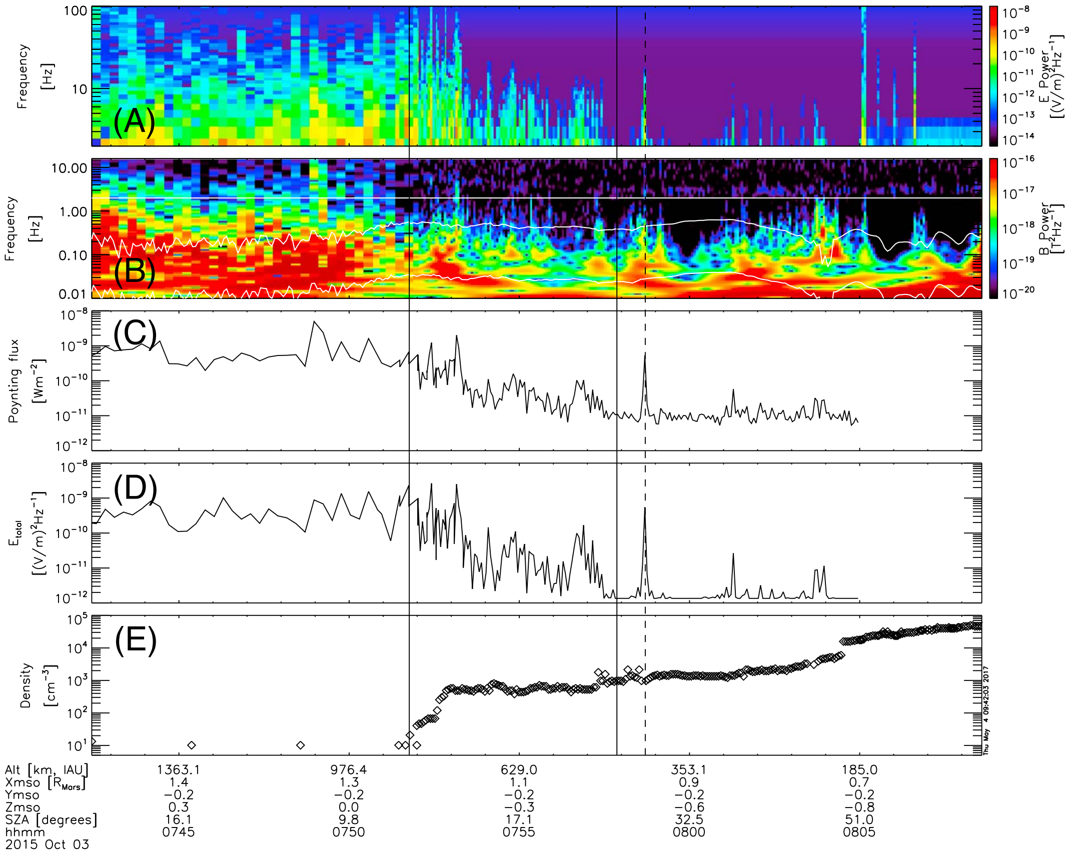

Figure 5. Example inbound periapsis pass from one of the 140 passes analyzed. (a) The electric field power spectrum between 2 and 100 Hz. (b) The magnetic field power spectrum between 0.01 and 16 Hz; the white horizontal line marks 2 Hz, and the other two white lines mark the proton and O^+ gyrofrequencies. (c) An estimate of the Poynting flux, as derived in section 3.2. (d) The total electric field wave power summed over the 2–100 Hz range. (e) The local electron density as derived from the LPW wave sounding measurements. The left and right solid vertical lines mark the top of the ionosphere, and the altitude to which electric field wave power is continuously observed to, respectively. The dashed vertical line marks an example of where an enhancement in wave power corresponds to a reduction in electron density; such events were not the focus of this study.

has recently been reported by *Fowler et al.* [2017]. Wave power is indeed observed to overlap with the upper ionosphere, and the results of this analysis are presented in section 4.2.

3.3. Solar Wind IMF Orientation

The third part of this study analyzed the distribution of 1-D electric and absolute magnetic field wave power throughout the Martian magnetosphere as functions of several upstream solar wind parameters. The solar wind is a primary energy input to the Martian system, and observations of how energy flows through the magnetosphere under varying upstream conditions can provide information about the dominant physical processes facilitating this transfer of energy. The statistical nature of this study (as opposed to a case-by-case study of individual shock crossings) again only allows for broad conclusions to be drawn in these analyses.

The upstream solar wind driver presented here is the solar wind interplanetary magnetic field (IMF) cone angle, defined as the angle between the solar wind flow and IMF. Several upstream Mach numbers (Alfvénic Mach number (V_a), sonic Mach number (M_s), magnetosonic Mach number (M_{ms})); proton beta (the ratio of proton particle pressure to solar wind pressure); and the solar wind density (N_{sw}) and velocity (V_{sw}) were also investigated, but we do not show results from these studies due to space limitations and leave this work for future publication.

The effects of the IMF cone angle on wave power distribution were investigated by analyzing parallel or antiparallel IMF conditions, compared to perpendicular IMF conditions. The IMF cone angles of 0° and 180° correspond to parallel ($-B_x$) and antiparallel ($+B_x$) IMF, respectively (relative to the solar wind flow);

90° is perpendicular IMF. The distribution of IMF cone angles (0° to 180°) was split into four quartiles (Q1 – Q4): Q1 spanned angles 0° – 71°; Q2 spanned 71° – 89°; Q3 spanned 89° – 107°, and Q4 spanned 107° – 180°. These values were chosen so that each quartile contained the same number of samples. Quartiles one and four correspond to $-B_x$ and $+B_x$ IMF, respectively. The middle two quartiles represent approximately perpendicular IMF. Statistical maps of wave power distribution were thus generated for quartiles Q1, Q2 + Q3, and Q4. The effects of IMF cone angle were determined by dividing statistical maps for the following quartiles: $\frac{Q1}{Q2+Q3}$ ($-B_x$) and $\frac{Q4}{Q2+Q3}$ ($+B_x$). No IMF orientations were exactly parallel or antiparallel to the solar wind velocity: the minimum, median, and maximum IMF values were 7°, 89° and 174°, respectively; 95% of the distribution lay between 30° and 150°.

3.4. Analysis Caveats

Here we discuss the chosen frequency ranges as outlined in section 3.1, using Figure 2 as an example. In the upstream solar wind, when the magnetic field is typically a few nanoteslas, wave power around 0.05 Hz is close to the local proton cyclotron frequency. In the magnetosheath, where magnetic field strengths of ~20 nT are more common, the local proton cyclotron frequency is closer to ~0.3 Hz. Wave power in the ULF (0.01 – 0.05 Hz) range is thus typically associated with heavier ion cyclotron frequencies, although the local proton cyclotron frequency can occur in this frequency range in the upstream solar wind. We do not choose a lower frequency range due to the extended window lengths required to capture such low-frequency oscillations; MAVEN's apoapsis velocity is ~1.5 km s^{-1} and spatial effects, such as passing through plasma boundaries, may start to significantly affect the observed power spectra under such long window lengths. The LF (1 – 5 Hz for MAG and 2 – 5 Hz for LPW) range was chosen as this is the lowest frequency range at which the LPW instrument can sample at; this range typically samples above the local proton cyclotron frequency except in cases where the magnetic field is particularly strong, ~50 nT. The magnetic field strength can reach values close to this in the magnetosheath, as seen in Figure 2f. The LF range thus likely samples harmonics of the local proton cyclotron frequency, although there are several other possible sources of waves that lie within this frequency range, as discussed in sections 5.1 and 5.2. The MF (5 Hz) range was chosen because electric field wave power tends to fall off quickly at frequencies greater than this when the spacecraft is in the solar wind. This choice was arbitrary, and similar analysis could be carried out for frequencies of 4 Hz, 6 Hz, or 4 – 6 Hz, for example. The most intense wave power within the bow shock and magnetosheath tends to peak close to this frequency as well. These features can be seen in Figures 2a and 2c. The HF (1 kHz – 5 kHz) range is at the typical electron cyclotron frequency with a wave power that is much more sporadic in nature as can be seen in Figures 2a and 2c.

Finally, we note a possible source of error accompanying this analysis method related to the identification of "real waves" versus "single events." As an example, waves in the local magnetic field are typically required to possess some number of oscillations to be classified as a real wave [e.g., *Brain et al.*, 2002; *Espley et al.*, 2004]. If MAVEN crosses a plasma boundary that has a spatial scale similar to, say, a 5 Hz wave in the magnetic field, then this single boundary crossing will appear as wave power in the 5 Hz band of the magnetic field power spectra. The same argument holds for the electric field power spectra. Given the difficulty associated with reliably identifying plasma boundaries in an autonomous manner (and indeed the number of plasma boundaries and regions observed in this study), we do not attempt to correct for this source of error.

4. Statistical Maps and Results

The following statistical maps are shown in the MSE frame. Maps were also produced in the MSO frame, but we do not show them here due to space limitations. Spatial coverage was significantly improved in the MSE frame, and the data reveal more definite structures. Various plasma boundaries and regions, for example, which are discussed below, are more clearly observed in the MSE frame. The overall trends that are described below are observed in both frames.

4.1. Electric and Magnetic Wave Power

Statistical maps in the MSE frame of electric field wave power for the LF, MF, and HF ranges are shown in Figure 6. Each row shows a specific frequency range (labeled on each color bar); Figures 6a, 6c, and 6e show the *X*-*Z* frame and Figures 6b, 6d, and 6f show the *X*-*Y* frame. We remind the reader that the binning method used is described in section 3 and Figure 4. Empirical boundaries for the bow shock and MPB as determined by *Vignes et al.* [2000] are overplotted as gray lines in the panels. Only bins that contained at least 10 data points have been used, with most bins typically containing a few thousand data points. The color bars span 3 orders

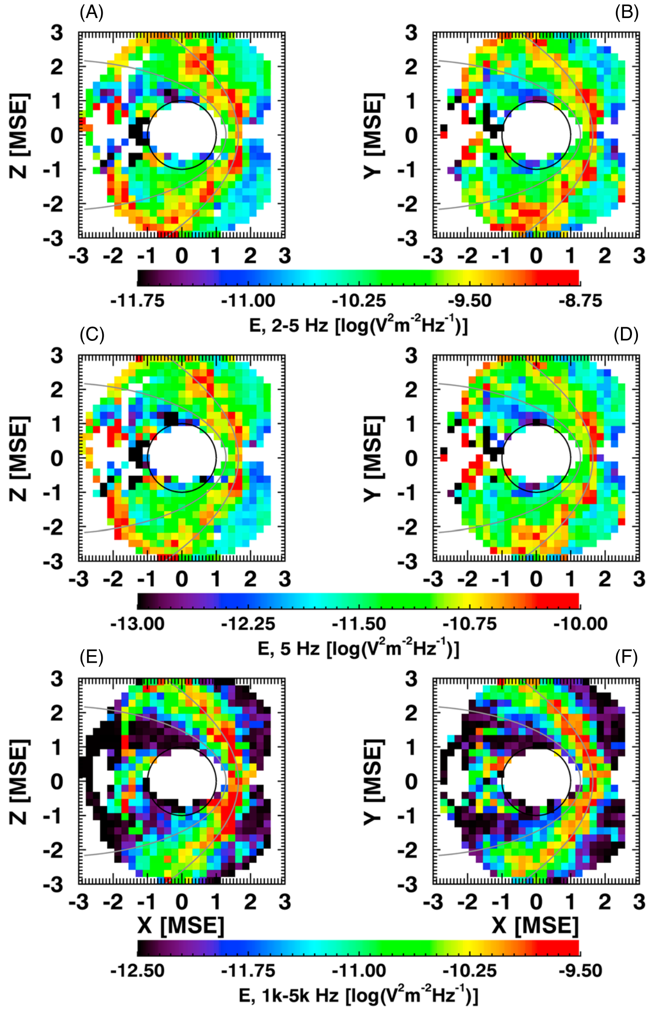

Figure 6. Statistical wave power distribution of the 1-D electric field, for altitudes greater than 600 km, for the LF ((a and b) 2–5 Hz), MF ((c and d) 5 Hz), and HF ((e and f) 1 kH–5 kHz) ranges. The statistical mean is used in Figures 6e and 6f due to the sporadic occurrence of wave power within the HF range. The results in Figures 6a and 6b may be due to low-frequency instrument noise, particularly in the magnetotail region (see sections 2.1.5 and 5).

of magnitude but start at different values, so that features can be observed in each frequency range. The LF range (Figures 6a and 6b) contains the most wave power, with the MF (Figures 6c and 6d) and HF (Figures 6e and 6f) ranges containing ~3–4 orders of magnitude less power. We also note that the HF range shows the statistical mean wave power as opposed to the statistical median wave power. Inspection of individual power spectra shows that wave power in the 1 kHz–5kHz range is sporadic in nature; when the median is used to bin the data, a "blank" map is obtained showing little wave power and no structure. Using the mean produces the map shown here; further discussion of the importance of this is left for later.

Wave power in the LF and MF ranges shows spatial structure, with peaks in wave power along the bow shock (Figures 6a–6d). Wave power decreases in the upstream solar wind, although there is some spill over from the bow shock into the upstream region—the upper edge of the bow shock is not sharp. Symmetric "horns" of enhanced wave power are observed upstream of the shock about the $Y = 0$ and $Z = 0$ lines, particularly for Figures 6a–6d. Downstream of the MPB wave power decreases, again with some overspill from the sheath. Wave power along the bow shock peaks at the subsolar point. The enhanced wave power in the central magnetotail is likely due to LF noise (as discussed in section 2.1.5) and represents the upper limit to wave power there. The HF wave power shown in Figures 6e and 6f shows the most structure, with the greatest power observed along the bow shock, peaking at the subsolar point. The upstream edge of the bow shock still shows overspill of wave power into the upstream region, but the lower boundary of the MPB is much clearer and sharper compared to the LF and MF ranges. In the flanks of the magnetotail, wave power is generally small but patches of enhancement exist close to planet in the central tail region. There is no obvious asymmetry in electric field wave power distribution in the Martian magnetosphere in the MSE frame, for all three of the frequency ranges shown here.

Statistical maps of the absolute magnetic field wave power are shown for the ULF, LF, and MF ranges in Figure 7. These maps follow the same layout as those for the electric field power spectra except that all three figures were produced using the statistical median of the data, and the color bar for the MF range covers 2 orders of magnitude only. The Martian magnetosphere is clearly visible in Figures 7a and 7b, with magnetic field wave power peaking in the sheath. The majority of wave power is at the subsolar point with significant power present just upstream of the shock front. The symmetric horns of wave power upstream of the shock are not as obvious as for the electric field but are still present in Figures 7a and 7b. There is also significant wave power throughout the magnetotail; the inner MPB is visible although this boundary is not sharp in the flanks

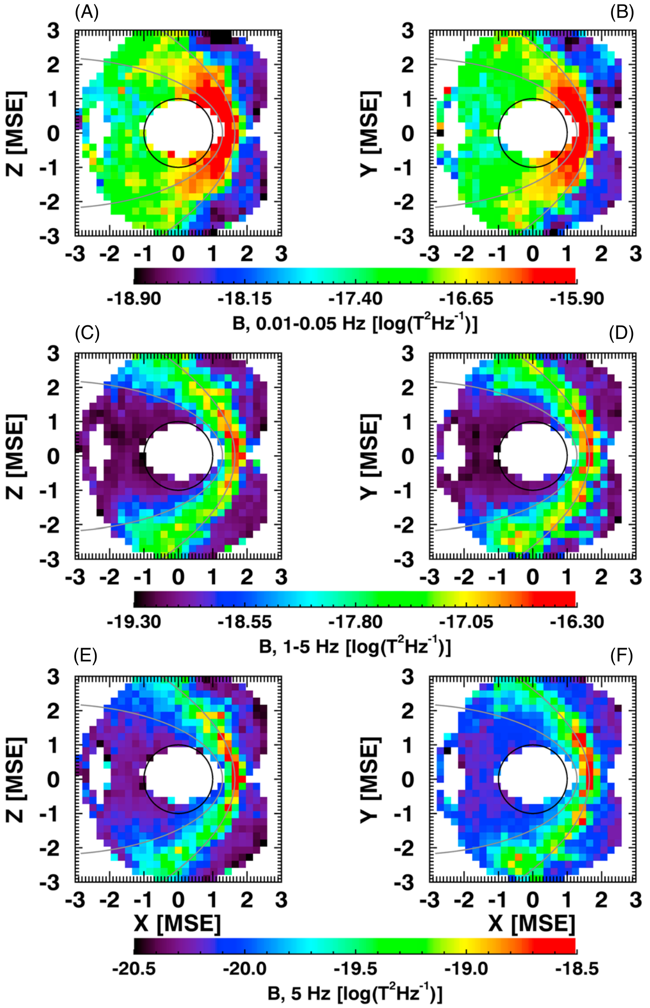

Figure 7. Statistical wave power of the absolute magnetic field strength, for altitudes greater than 600 km, for the ULF ((a and b) 0.01–0.05 Hz), LF ((c and d) 1–5 Hz), and MF ((e and f) 5 Hz) ranges. Note that the color bar ranges differ for each set of plots, with substantially more wave power present in the ULF than LF and MF ranges.

of the tail. Clear structure is present in the LF range shown in Figures 7c and 7d with wave power peaking at the subsolar point and along the bow shock, as apposed to within the sheath for the ULF range. The majority of wave power is at the bow shock and within the sheath—there is little power in the tail region. The inner MPB is now clear and fairly sharp. Wave power in the MF range shown in Figures 7e and 7f is again structured, with wave power focused along the bow shock and outer sheath regions. Peak wave power is again at the subsolar point. The MPB is visible, but wave power falls off within the inner sheath region before reaching this boundary, particularly in the flanks of the sheath. Wave power in the ULF range is at least an order of magnitude greater than the LF and MF ranges, highlighted by the difference in color bar scales used for each set of plots in Figure 7.

4.2. Wave Power Reaching the Upper Ionosphere

Results of the statistical analysis of the 140 inbound periapsis passes described in section 3.2 are shown in Figure 8. Electric field wave power was observed within the ionosphere for all 140 cases, as shown in Figure 8a. The distributions of these top and *E* field boundary altitudes are shown in Figures 8b and 8c. The penetration depth that wave power was observed to, within the ionosphere, is shown in Figure 8d. This was defined as the difference in top and *E* field boundary altitudes. The most likely depth was between 150 and 200 km; wave power was observed at depths greater than 300 km for 15% of periapsis passes and down to nearly 600 km in the most extreme cases. The distribution of integrated electron density at the *E* field boundary is shown in Figure 8e. The integrated electron density was calculated by integrating the electron density between the upper and *E* field boundaries, as a function of spacecraft altitude at each measurement point. Continuous wave power was most likely to be observed at integrated densities of between about $10^{9.5}$ and 10^{10} cm^{-2}. A sharp cutoff exists after this peak, and continuous wave power was never observed above integrated densities of about $10^{10.8}$ cm^{-2}. Short, discrete bursts of wave power were observed at higher integrated densities, as seen in Figure 5a, but were not investigated in this study. The *E* field boundary was not observed below altitudes of 170 km, and this is shown by the distribution of *E* field boundary altitudes in Figure 8c. The most likely *E* field boundary altitude was just below 400 km, although the shape of the distribution suggests that the actual value may be around 300 km, were a greater number of periapsis passes to be included in the analysis. The distributions of total electric field wave power, and Poynting flux, at the top boundary, are shown as the black and blue dashed lines, respectively in Figure 8f. Poynting fluxes at the top layer were most commonly observed between 10^{-10} and 10^{-9} Wm^{-2}, although Poynting fluxes greater than 10^{-8} Wm^{-2} were also observed. The electric field wave power distribution shows similar behavior, albeit with a slightly wider distribution.

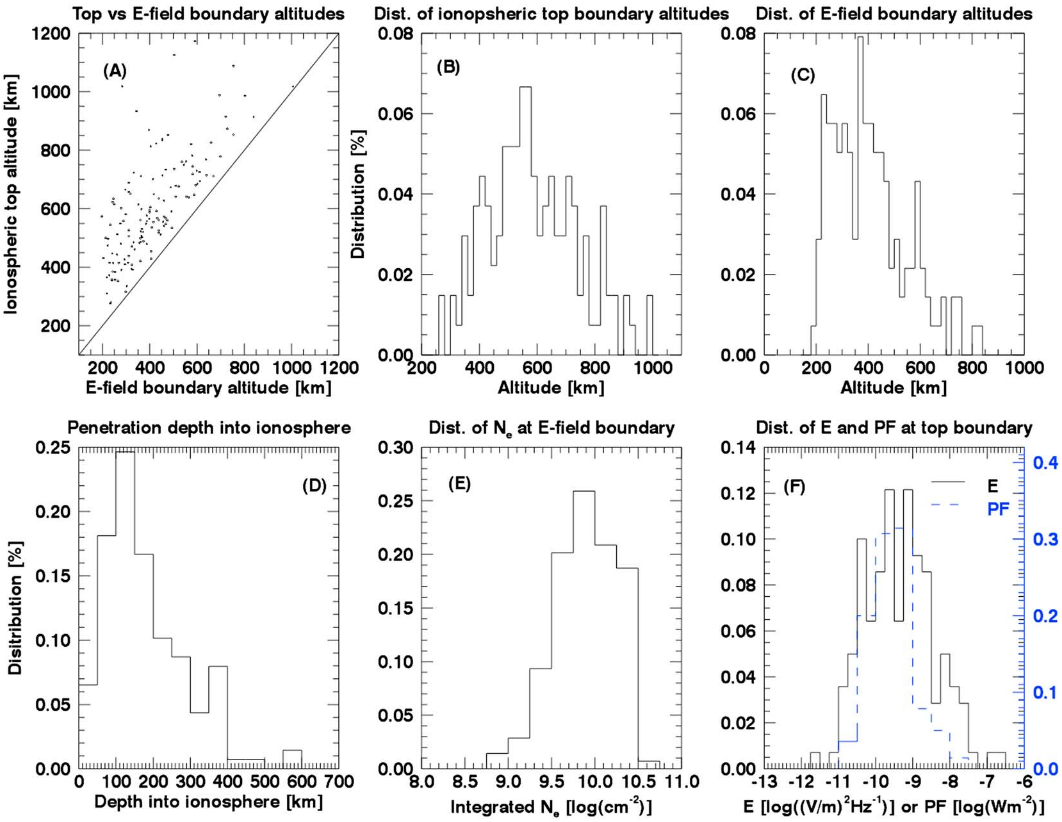

Figure 8. Results of the statistical study of 140 dayside periapsis passes. The “top” boundary is when the spacecraft first observes the upper ionosphere; the “*E* field” boundary is when electric field wave power is no longer observed. (a) A scatterplot of top versus *E* field boundaries; the solid line marks 1:1. (b) The distribution of top boundary altitudes; (c) The distribution of *E* field boundary altitudes; (d) The distribution of penetration depths into the ionosphere that electric field wave power was observed. (e) The distribution of integrated electron densities, integrated between the top and *E* field boundaries. (f) The distributions of Poynting flux and electric field wave power at the top boundary.

Hartinger et al. [2013] investigated correlations between observed Poynting vectors and the local magnetic field vector in the terrestrial magnetosphere. They reported that for lower frequencies in their study (6 and 18 mHz), energy was transferred mostly parallel to the local magnetic field in the upstream terrestrial magnetosphere, suggesting that Joule dissipation in the terrestrial ionosphere may be an important sink for the observed ULF waves in their study. We attempted a similar analysis using the MAVEN 1-D electric field measurements in this study, investigating Poynting fluxes as a function of the angle between the 1-D electric field measurement and the local magnetic field vector. This angle varies with time due to changes in the local magnetic field vector and changes in the spacecraft orientation. No obvious correlations were found between the size of this angle and the observed Poynting fluxes. A full 3-D electric field measurement is required to confirm these (lack of) correlations.

4.3. Solar Wind Effects on Wave Power Distribution

The distribution of 1-D electric and absolute magnetic field wave power in the *X*-*Y* MSE plane, for the MF and LF ranges, respectively, is shown in Figure 9. The ratio of electric (magnetic) wave power, for parallel compared to perpendicular IMF conditions, is shown in Figure 9a (Figure 9b), and for antiparallel compared to perpendicular IMF conditions, in Figure 9c (Figure 9d). The color bar is the log of the ratio for these conditions. For parallel IMF conditions, electric and magnetic wave power is enhanced by factors of 20–30 on the dawnside ($-Y$) and reduced by similar amounts on the duskside ($+Y$). The opposite is observed for antiparallel IMF conditions. Magnetic field wave power is roughly constant within the magnetotail; electric field wave power shows more variation within the magnetotail, but this may be a result of low-frequency noise that can contaminate the MF range within the magnetotail (see section 2.1.5). The frequency ranges presented showed the strongest variations in wave power with respect to solar wind IMF conditions.

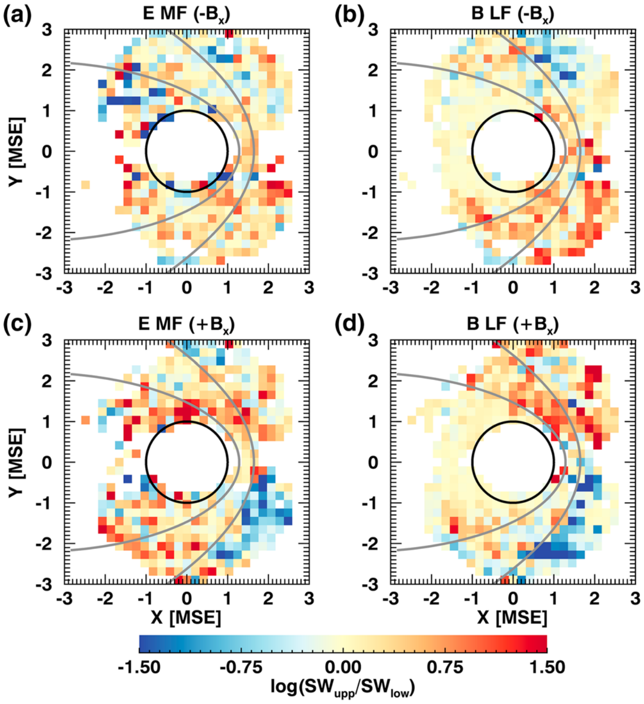

Figure 9. The log-scale ratio of absolute MF (5 Hz) 1-D electric and LF (1–5 Hz) magnetic wave power, for parallel compared to perpendicular solar wind IMF ((a and b) "$-B_X$") and antiparallel compared to perpendicular solar wind IMF ((c and d) "$+B_X$").

5. Interpretation and Discussion

We first discuss the statistical maps presented in Figures 6 and 7; discussion of wave power overlaps, with the upper ionosphere, and the effect of the IMF on wave power distribution, follows in sections 5.6 and 5.7. Electric field wave power in the HF range was observed much more sporadically than in the MF range, but when present, this HF power was comparable to or greater than that in the LF and MF ranges, as seen in Figure 6. This suggests that electron-driven waves occur more sporadically in the Martian magnetosphere than ion-driven waves but, when present, are able to contribute significant amounts of power. Ion thermalization is typically the dominant dissipation mechanism within collisionless shocks; however, electron heating still occurs via current-driven instabilities at the shock front [*Kivelson and Russell*, 1995]. The sporadic occurrence of electron-driven waves may thus indicate times when electron heating is of increased importance.

Enhanced electric field wave powers in the tail observed in this study (particularly in the LF and MF ranges) are likely a result of low-frequency noise (section 2.1.5), and because of this we do not discuss the tail region further with respect to the LF and MF electric field power spectra.

5.1. Wave Power in the Magnetosheath

Various plasma boundaries and regions are visible in the statistical maps of electric and magnetic field wave power presented throughout this study. Magnetic field wave power, in particular, shows obvious structure in all ranges (Figure 7). Wave power peaks within the sheath in the ULF range, and this is a result of ion thermalization within the sheath to aid in the dissipation of upstream solar wind kinetic energy [e.g., *Papadopoulos*, 1971; *Auer et al.*, 1971; *Burgess et al.*, 1989; *Bale et al.*, 2005, 1989].

It has been noted by *Moses et al.* [1988], for example, that the standoff distance of the Martian shock is small compared to the typical ion plasma length scales in the Martian magnetosphere, meaning that full thermalization of the solar wind plasma is unlikely to occur within the magnetosheath. Thermalization typically occurs at the length and time scales associated with the local ion gyrofrequencies, which at the Martian shock are closest to the ULF range analyzed in this study. There is no obvious drop in magnetic field wave power in Figures 7a and 7b between the sheath and lower altitude limit in this study (600 km) at the subsolar point, supporting the theory that there is not enough space between the shock and planetary ionosphere for the shocked solar wind plasma to fully thermalize there. There has been extensive research regarding the thermalization of ions and electrons at the terrestrial shock [e.g., *Feldman et al.*, 1983; *Burgess et al.*, 1989; *Sckopke et al.*, 1990; *Bale et al.*, 2002]; such detailed studies are only now possible at Mars because of the instrumentation carried by MAVEN. Previous spacecraft flown at Mars have, however, allowed modeling studies of the system to be undertaken. *Brecht et al.* [1993], for example, ran three-dimensional hybrid model simulations of the dayside Mars-solar wind interaction region. They compared their results with Phobos 2 plasma data and concluded that ions would not fully thermalize before encountering the Martian ionosphere, particularly in the subsolar region. The results presented in this study support these earlier hypotheses, demonstrating that solar wind ions are unlikely to fully thermalize within the Martian subsolar sheath region.

5.2. Wave Power at and Immediately Upstream of the Shock Front

Wave power is also observed to peak along the bow shock, particularly at the subsolar point: this occurs in the LF, MF, and HF ranges for electric field and the LF and MF ranges for magnetic field. This wave power, and the “smearing out” of the shock front boundary observed in the statistical maps presented here, is likely products of several sources: the movement of the shock front in response to changing upstream solar wind conditions [e.g., *Slavin et al.*, 1991; *Vignes et al.*, 2000; *Brain et al.*, 2005; *Trotignon et al.*, 2006; *Edberg et al.*, 2009a, 2009b; *Halekas et al.*, 2016]; the motion of reflected ions at the shock front that aid in the dissipation of upstream solar wind kinetic energy [e.g., *Paschmann et al.*, 1981; *Gosling et al.*, 1982; *Burgess et al.*, 1989]; over and under shoots in the magnetic field immediately downstream of the collisionless shock [e.g., *Livesey et al.*, 1982; *Mellott and Livesey*, 1987]; and electromagnetic waves [e.g., *Grard et al.*, 1989; *Brain et al.*, 2002; *Mazelle et al.*, 2004]. The exact relative contributions of these sources cannot be determined without in-depth analysis on an orbit-by-orbit basis; knowledge of whether the spacecraft is magnetically connected to the shock, for example, provides information on whether ions reflected from the shock can be observed or not. Such detailed analysis on a data set this large is outside the scope of this study and is not undertaken here.

Whistler waves have been observed at the Martian shock at about 1–2 Hz and are thought to be generated within the sheath before propagating into the upstream region [*Grard et al.*, 1989; *Brain et al.*, 2002] and likely contribute to the wave power observed at the shock front and immediately upstream of it in Figures 6a, 6b, and 7a–7d. *Brain et al.* [2002] also analyzed wave power in the range 0.04–0.1 Hz; the absolute magnetic field wave power peaked within the sheath, at similar absolute powers, as observed in the ULF range in this study.

5.3. Wave Power at the MPB

The MPB is observed in the electric and magnetic field power spectra. There is again variation in the location of this boundary, most likely caused by varying upstream solar wind conditions. Typically, wave power falls off downstream of the MPB, particularly in the tail region, suggesting that little dissipation of upstream energy occurs in this region, as expected. *Espley et al.* [2004] analyzed magnetic field data from the MGS spacecraft and concluded that oscillations below the local proton frequency decreased in amplitude downstream of the MPB within the magnetotail region, agreeing with results from this study. *Bertucci et al.* [2004] used MGS magnetometer data to report similar ULF waves either side of the MPB, which are also observed in this study.

5.4. Upstream Wave Power

Waves at the local proton cyclotron frequency are known to exist upstream of the bow shock at Mars [e.g., *Russell et al.*, 1990; *Bertucci et al.*, 2013; *Brain et al.*, 2005] and are the probable cause of upstream wave power observed in the ULF and LF ranges in Figures 6a, 6b, and 7a–7d. Such waves are likely the product of ion cyclotron like waves produced by the ionization of the neutral corona. An ion-ion beam instability can form as a result of the interaction between the newly ionized, approximately stationary coronal particles, and the solar wind flow [e.g., *Delva et al.*, 2011]. Although ion cyclotron waves are most frequently right-handed wave modes in the plasma rest frame, Doppler shift effects caused by the solar wind flow velocity can cause such waves to be observed as left-handed waves in the spacecraft frame [e.g., *Mazelle and Neubauer*, 1993]. This study did not analyze the magnetic field data in such detail, but we note these effects for future reference. Symmetric horns of electric and magnetic wave power are observed upstream of the shock in Figures 6a–6d, 7a, and 7b. Without more detailed information it is difficult to determine the cause of these structures; however, they may represent the statistical extent of the dawn and dusk foreshock regions.

The statistical maps presented in this study support the conclusion drawn by *Delva et al.* [2011] that upstream cyclotron wave generation occurs at the initial ionization point of the neutral corona, as opposed to a later point in time once the ionized particle has been picked up by the solar wind. There is no obvious asymmetry in the $+Z$ direction in Figures 6 and 7, which are presented in the MSE frame. If wave generation were to occur after the initial ionization, an asymmetry would be present in the $+Z$ direction, due to the large gyroradii of ionized coronal particles that are typically on the order of the planetary radius or greater at Mars. Pickup ions are subsequently accelerated over the planet in the $+Z$ MSE direction, producing what is known as the polar plume [e.g., *Lundin et al.*, 2006a, 2006b; *Curry et al.*, 2015; *Dong et al.*, 2015]. The relatively large coronal densities at Mars mean that the generation of upstream cyclotron waves of newly ionized coronal particles occurs for many different configurations of solar wind velocity and magnetic field, and it is thus not surprising to observe these upstream waves in Figures 6 and 7, where all solar wind conditions have been included in the analysis.

5.5. Wave Power in the Magnetotail

The general lack of wave power within the magnetotail is presumable because this region is typically not magnetically connected to the shock front, sheath, or solar wind, which are the primary generation regions for wave power observed in the magnetosphere. Magnetic ULF wave power in the magnetotail is ~2 orders of magnitude greater than for the LF and MF ranges there, and significant electric field wave power in the HF range is also observed in the tail. These phenomena may be related to large-scale structures such as current sheet crossings, which lie outside the scope of this work.

5.6. Statistics of Wave Power Observed in the Ionosphere

Electric field wave power was observed in the upper ionosphere for all 140 cases comprising Figure 8. Assuming that wave power propagates from the sheath toward the planet, these observations strongly support the theory put forward by *Moses et al.* [1988] that the shocked solar wind plasma does not have space to fully thermalize before encountering the upper ionosphere at Mars. Wave power generated at the Mars-solar wind interaction that propagates into the upper ionosphere may thus provide energy for ionospheric heating, as is known to occur at Venus [e.g., *Taylor et al.*, 1979; *Scarf et al.*, 1980; *Shapiro et al.*, 1995]. Estimates of Poynting flux in the 2–16 Hz range at the upper ionospheric boundary ranged from $\sim 10^{-11}-10^{-8}$ $\mathrm{Wm^{-2}}$ (Figure 8f). These estimates are at the lower end of estimates provided by *Ergun et al.* [2006] (based solely on MGS magnetic field data and calculated at the approximate local O^+ gyrofrequency, 0.04 Hz) and are ~3–4 orders of magnitude smaller than heat fluxes derived from energy balance in the lower ionosphere (below ~350 km) by *Chen et al.* [1978], *Choi et al.* [1998], and *Matta et al.* [2014]. The estimates from this study are lower than previously published estimates likely due to the limited frequency range at which the LPW and MAG instruments overlap. Significant wave power is observed below 2 Hz in the magnetic field (and likely electric field, but MAVEN cannot measure these frequencies); Figure 7 shows that magnetic field wave power is 2–3 orders of magnitude greater in the 0.01–0.05 Hz range compared to the 1–5 Hz range.

Recently, *Fowler et al.* [2017] reported correlations between electric field wave power between 2 Hz and 100 Hz and electron temperatures, within the dayside ionosphere at Mars, showing that enhancements in electron temperature of up to 1000 K were observed for the largest wave powers. The electric field wave power observed in this study (that is assumed to propagate from the sheath toward the planet) is a likely source of the wave power observed in the *Fowler et al.* [2017] study.

The sharp cutoff in integrated densities above which no wave power is observed (Figure 8e) suggests that the ionospheric density plays a crucial role in absorbing the observed wave energy. Somewhat surprisingly, no correlations were observed between integrated electron densities at the E field boundary and estimated Poynting flux at the upper boundary (not shown here due to space limitations). This is somewhat counter intuitive, given that one might expect a larger integrated ionospheric density to be required to absorb a larger energy input. Two possible causes for this lack of correlation are the limited frequency range over which Poynting flux is estimated (the Poynting fluxes are thus underestimated) and the fact that MAVEN is unlikely to travel parallel to the Poynting vector within the ionosphere (MAVEN does not observe the “evolution” of the same original input energy as it travels through the ionosphere).

The statistical study also demonstrates the highly variable nature of the Martian ionosphere, even on the dayside of the planet. The top ionospheric boundary was observed between altitudes of 200 and 1000 km (Figure 8b). This variation in top boundary altitude is to first order driven by variations in upstream solar wind conditions; pressure balance between the incident solar wind flow and the draped magnetic fields determines how compressed the underlying ionosphere will become [e.g., *Crider et al.*, 2003].

5.7. Wave Power as a Function of Upstream Solar Wind IMF Cone Angle

The analysis of the distribution of wave power within the Martian magnetosphere, as a function of solar wind IMF orientation, assumed that only the solar wind IMF varied and that all remaining solar wind parameters remained constant. This is true for some parameters, but not others, and correlations are observed between certain upstream parameters. These correlations have been investigated, and it was found that the distributions of all other upstream solar wind parameters (investigated in this study, as outlined in section 3.3) were roughly constant regardless of IMF direction. Thus, the statistical variations in wave power with respect to solar wind IMF are likely driven to first order by these changes in IMF direction and not a different upstream parameter. Due to space limitations, we do not show examples of the investigated correlations here.

The IMF follows on average a Parker spiral configuration leading to a typical Parker spiral angle (the angle between the IMF and the direction radially outward from the Sun) of ∼56° at Mars [e.g., *Parker*, 1963; *Thomas and Smith*, 1980; *Ma et al.*, 2004]. The Parker spiral angle determines which parts of the Martian shock the upstream IMF is magnetically connected to. The statistical distribution of absolute electric and magnetic wave power varies with parallel or antiparallel IMF conditions, shown in Figure 9. In the MSE frame, the solar wind magnetic field points in the dusk ($+Y$) direction. If the IMF B_x component is negative, i.e., pointing antisunward (corresponding to parallel IMF), the spacecraft is more likely to be magnetically connected to the shock front on the dawn ($-Y$) side of Mars, in the MSE frame. Thus, the enhanced wave power observed just upstream of the shock front on the $-Y$ side of Figures 9a and 9b is likely associated with plasma instabilities within the foreshock region, as MAVEN is more likely to be magnetically connected to the shock here. The same enhancements in wave power are observed on the dusk ($+Y$) side of Mars under antiparallel IMF conditions, as expected.

Magnetic wave power in the magnetotail (Figures 9b and 9d) is roughly constant with changing IMF conditions and this is expected—changes in IMF direction to first order affect the location at which the spacecraft can be magnetically connected to the shock front and not the magnetotail. Electric wave power in the magnetotail (Figures 9a and 9c) is more variable, and this is likely due to low-frequency noise that can be present in the tail region for the electric field MF range shown here.

This third study is meant as a demonstration that expected statistical behaviors are present in the new data sets provided by MAVEN. Individual, detailed case studies are required to dig out the wealth of information present here.

5.8. Long-Term Trends

The data analyzed in this study span 14.5 months, and any seasonal trends that may be present have been averaged across. It has been observed, for example, that the occurrence of upstream cyclotron waves correlates with the neutral coronal density [*Bertucci et al.*, 2013], which is in turn a function of solar cycle and season [e.g., *Kim et al.*, 1998; 2009]. It is left for future work to investigate such temporal trends on the distribution of electric and magnetic wave power in the Martian magnetosphere.

6. Conclusions

A statistical study of ∼14.5 months of absolute electric and magnetic field wave power spectra observed by the MAVEN spacecraft has produced a much more comprehensive study of wave power distribution within the Martian magnetosphere than has previously been possible. The key conclusions from this study are as follows:

1. The lowest-frequency ranges contained the most wave power for the absolute electric and magnetic field power spectra (Figures 6 and 7). Various plasma boundaries and regions are clearly evident in the statistical maps, including the magnetic pile up boundary (MPB), bow shock, and magnetosheath. Enhancements in wave power at these boundaries show regions important for the dissipation of solar wind energy incident to the planetary obstacle. Increases of wave power observed in the sheath, particularly in the ULF range (0.01–0.05 Hz) analyzed in this study, most likely represent the partial thermalization of ions in this region (see point 2 below).
2. Statistical maps of electric and magnetic wave power suggest that the sheath does not appear large enough to allow full ion thermalization of the shocked solar wind plasma, as has been predicted by, for example, *Moses et al.* [1988]. A statistical study of 140 dayside periapsis passes showed that wave power and estimated Poynting fluxes (within the 2–16 Hz range) reached the upper ionosphere for all 140 cases (Figure 8a).

Assuming that wave power generated within the sheath propagates toward the planet, electric field wave power (above 2 Hz) was observed to propagate to typical depths of 100–200 km within the ionosphere and up to nearly 600 km in rare cases. Magnetic variations above 2 Hz were essentially at the noise level of the instrument within the ionosphere; significant variations are present at lower frequencies, which lie outside the measurement range of the electric field data.

3. Wave power observed within the upper ionosphere can provide an ionospheric heating source. Wave power was not observed for integrated electron densities greater than $10^{10.8}$ cm^{-2}.
4. Estimated Poynting fluxes in the frequency range 2–16 Hz are observed to lie between $\sim10^{-11}$ and 10^{-8} Wm^{-2} (Figure 8f) at the upper ionospheric boundary. Such values lie at the lower end of estimates provided by *Ergun et al.* [2006] and are ∼3–4 orders of magnitude smaller than estimates from *Chen et al.* [1978], *Choi et al.* [1998], and *Matta et al.* [2014]. The underestimates in this study are likely due to the limited frequency range over which the Poynting flux can be estimated (2–16 Hz) using MAVEN data; magnetic field variations typically increase by 2–3 orders of magnitude below 2 Hz (Figure 7).
5. Variations in the distribution of electric and magnetic field wave power were observed as a function of average upstream solar wind IMF orientation (Figure 9). The statistical nature of this study makes it hard to conclusively determine the cause(s) of these variations, but changes in the upstream IMF orientation strongly affect whether the spacecraft is magnetically connected to the shock front or not, likely driving the observed differences. Upstream from the shock, enhancements in wave power of factors up to 20–30 are observed when the spacecraft is likely magnetically connected to the shock front, compared to when it is not.
6. Detailed caveats concerning the Langmuir Probe and Waves electric field wave spectra data set from the Mars Atmosphere and Volatile EvolutioN mission are presented in the first half of this paper. Example spectra, including discussed caveats, are presented in Figures 2 and 3 and are meant as aids to researchers who wish to analyze this extensive data set.

Acknowledgments
Work at LASP and SSL was supported by NASA funding for the MAVEN project through the Mars Exploration Program, under grant number NNH10CC04C. Data used in this study are available on the NASA Planetary Data System, via https://pds.nasa.gov/. E.R.C. was supported by NASA through the Einstein Fellowship Program, grant PF6-170150. We would like to thank the anonymous reviewers who took the time and effort to evaluate this manuscript and to help improve it through the peer review process. E. R. Coughlin is an Einstein Fellow.

References

Acuna, M., et al. (1998), Magnetic field and plasma observations at Mars: Initial results of the Mars Global Surveyor mission, *Science*, *279*(5357), 1676–1680.

Andersson, L., R. Ergun, G. Delory, A. Eriksson, J. Westfall, H. Reed, J. McCauly, D. Summers, and D. Meyers (2015), The Langmuir Probe and Waves (LPW) instrument for MAVEN, *Space Sci. Rev.*, *195*(1–4), 173–198.

Andrews, D., L. Andersson, G. Delory, R. Ergun, A. Eriksson, C. Fowler, T. McEnulty, M. Morooka, T. Weber, and B. Jakosky (2015), Ionospheric plasma density variations observed at Mars by MAVEN/LPW, *Geophys. Res. Lett.*, *42*, 8862–8869, doi:10.1002/2015GL065241.

Auer, P., R. Kilb, and W. Crevier (1971), Thermalization in the Earth's bow shock, *J. Geophys. Res.*, *76*(13), 2927–2939.

Bale, S., A. Hull, D. Larson, R. Lin, L. Muschietti, P. Kellogg, K. Goetz, and S. Monson (2002), Electrostatic turbulence and Debye-scale structures associated with electron thermalization at collisionless shocks, *Astrophys. J. Lett.*, *575*(1), L25.

Bale, S., et al. (2005), Quasi-perpendicular shock structure and processes, *Space Sci. Rev.*, *118*(1-4), 161–203.

Bertucci, C., C. Mazelle, D. Crider, D. Mitchell, K. Sauer, M. Acuña, J. Connerney, R. Lin, N. Ness, and D. Winterhalter (2004), MGS MAG/ER observations at the magnetic pileup boundary of Mars: Draping enhancement and low frequency waves, *Adv. Space Res.*, *33*(11), 1938–1944.

Bertucci, C., F. Duru, N. Edberg, M. Fraenz, C. Martinecz, K. Szego, and O. Vaisberg (2011), The induced magnetospheres of Mars, Venus, and Titan, *Space Sci. Rev.*, *162*(1–4), 113–171.

Bertucci, C., N. Romanelli, J. Chaufray, D. Gomez, C. Mazelle, M. Delva, R. Modolo, F. González-Galindo, and D. Brain (2013), Temporal variability of waves at the proton cyclotron frequency upstream from Mars: Implications for Mars distant hydrogen exosphere, *Geophys. Res. Lett.*, *40*, 3809–3813, doi:10.1002/grl.50709.

Bonifazi, C., G. Moreno, A. Lazarus, and J. Sullivan (1980), Deceleration of the solar wind in the Earth's foreshock region: ISEE 2 and IMP 8 observations, *J. Geophys. Res.*, *85*(A11), 6031–6038.

Brain, D., F. Bagenal, M. Acuna, J. Connerney, D. Crider, C. Mazelle, D. Mitchell, and N. Ness (2002), Observations of low-frequency electromagnetic plasma waves upstream from the Martian shock, *J. Geophys. Res.*, *107*(A6), 1076, doi:10.1029/2000JA000416.

Brain, D., J. Halekas, R. Lillis, D. Mitchell, R. Lin, and D. Crider (2005), Variability of the altitude of the Martian sheath, *Geophys. Res. Lett.*, *32*, L18203, doi:10.1029/2005GL023126.

Brecht, S. H., J. R. Ferrante, and J. Luhmann (1993), Three-dimensional simulations of the solar wind interaction with Mars, *J. Geophys. Res.*, *98*(A2), 1345–1357.

Burgess, D., W. Wilkinson, and S. Schwartz (1989), Ion distributions and thermalization at perpendicular and quasi-perpendicular supercritical collisionless shocks, *J. Geophys. Res.*, *94*(A7), 8783–8792.

Chen, R., T. Cravens, and A. Nagy (1978), The Martian ionosphere in light of the Viking observations, *J. Geophys. Res.*, *83*(A8), 3871–3876.

Choi, Y., J. Kim, K. Min, A. Nagy, and K. Oyama (1998), Effect of the magnetic field on the energetics of Mars ionosphere, *Geophys. Res. Lett.*, *25*(14), 2753–2756.

Connerney, J., J. Espley, P. Lawton, S. Murphy, J. Odom, R. Oliversen, and D. Sheppard (2015), The MAVEN magnetic field investigation, *Space Sci. Rev.*, *195*, 257–291, doi:10.1007/s11214-015-0169-4.

Crider, D. H., D. Vignes, A. M. Krymskii, T. K. Breus, N. F. Ness, D. L. Mitchell, J. A. Slavin, and M. H. Acuña (2003), A proxy for determining solar wind dynamic pressure at Mars using Mars Global Surveyor data, *J. Geophys. Res.*, *108*(A12), 1461, doi:10.1029/2003JA009875.

Curry, S. M., et al. (2015), Response of Mars O^+ pickup ions to the 8 March 2015 ICME: Inferences from MAVEN data-based models, *Geophys. Res. Lett.*, *42*, 9095–9102, doi:10.1002/2015GL065304.

Delva, M., C. Mazelle, and C. Bertucci (2011), Upstream ion cyclotron waves at Venus and Mars, *Space Sci. Rev.*, *162*(1–4), 5–24.

Dong, Y., X. Fang, D. Brain, J. McFadden, J. Halekas, J. Connerney, S. Curry, Y. Harada, J. Luhmann, and B. Jakosky (2015), Strong plume fluxes at Mars observed by MAVEN: An important planetary ion escape channel, *Geophys. Res. Lett*, *42*, 8942–8950, doi:10.1002/2015GL065346.

Edberg, N., M. Lester, S. Cowley, D. Brain, R. Modolo, M. Fränz, and S. Barabash (2009a), Plasma boundary variability at Mars as observed by Mars Global Surveyor and Mars Express, *Ann. Geophys.*, *27*, 3537–3550.

Edberg, N., et al. (2009b), Rosetta and Mars Express observations of the influence of high solar wind pressure on the Martian plasma environment, *Ann. Geophys.*, *27*, 4533–4545. Copernicus GmbH.

Ergun, R., L. Andersson, W. Peterson, D. Brain, G. Delory, D. Mitchell, R. Lin, and A. Yau (2006), Role of plasma waves in Mars' atmospheric loss, *Geophys. Res. Lett.*, *33*, L14103, doi:10.1029/2006GL025785.

Ergun, R., et al. (2008), Eigenmode structure in solar-wind Langmuir waves, *Phys. Rev. Lett.*, *101*(5), 051101.

Ergun, R., M. Morooka, L. Andersson, C. Fowler, G. Delory, D. Andrews, A. Eriksson, T. McEnulty, and B. Jakosky (2015), Dayside electron temperature and density profiles at Mars: First results from the MAVEN Langmuir Probe and Waves instrument, *Geophys. Res. Lett.*, *42*, 8846–8853, doi:10.1002/2015GL065280.

Espley, J., P. Cloutier, D. Brain, D. Crider, and M. Acuña (2004), Observations of low-frequency magnetic oscillations in the Martian magnetosheath, magnetic pileup region, and tail, *J. Geophys. Res.*, *109*, A07213, doi:10.1029/2003JA010193.

Fairfield, D. (1971), Average and unusual locations of the Earth's magnetopause and bow shock, *J. Geophys. Res.*, *76*(28), 6700–6716.

Feldman, W., R. Anderson, S. Bame, S. Gary, J. Gosling, D. McComas, M. Thomsen, G. Paschmann, and M. Hoppe (1983), Electron velocity distributions near the Earth's bow shock, *J. Geophys. Res.*, *88*(A1), 96–110.

Fowler, C., et al. (2017), Correlations between enhanced electron temperatures and electric field wave power in the Martian ionosphere, *Geophys. Res. Lett.*, *44*, doi:10.1002/2017GL073387.

Gary, S. P. (1991), Electromagnetic ion/ion instabilities and their consequences in space plasmas: A review, *Space Sci. Rev.*, *56*(3–4), 373–415.

Gosling, J., M. Thomsen, S. Bame, W. Feldman, G. Paschmann, and N. Sckopke (1982), Evidence for specularly reflected ions upstream from the quasi-parallel bow shock, *Geophys. Res. Lett.*, *9*(12), 1333–1336.

Grard, R., A. Pedersen, S. Klimov, S. Savin, A. Skalsky, J. Trotignon, and C. Kennel (1989), First measurements of plasma waves near Mars, *Nature*, *341*(6243), 607–609.

Gringauz, K. (1976), Interaction of solar wind with Mars as seen by charged particle traps on MARS 2, 3, and 5 satellites, *Rev. Geophys.*, *14*(3), 391–402.

Halekas, J., E. Taylor, G. Dalton, G. Johnson, D. Curtis, J. McFadden, D. Mitchell, R. Lin, and B. Jakosky (2015), The solar wind ion analyzer for MAVEN, *Space Sci. Rev.*, *195*, 125–151, doi:10.1007/s11214-013-0029-z.

Halekas, J., et al. (2016), Structure, dynamics, and seasonal variability of the Mars-solar wind interaction: MAVEN solar wind ion analyzer in-flight performance and science results, *J. Geophys. Res. Space Physics*, *122*, 547–578, doi:10.1002/2016JA02316.

Hartinger, M., M. Moldwin, K. Takahashi, J. Bonnell, and V. Angelopoulos (2013), Survey of the ULF wave Poynting vector near the Earth's magnetic equatorial plane, *J. Geophys. Res. Space Physics*, *118*, 6212–6227, doi:10.1002/jgra.50591.

Jakosky, B., et al. (2015), The Mars Atmosphere and Volatile EvolutioN (MAVEN) mission, *Space Sci. Rev.*, *195*, 3–48.

Kim, J., A. F. Nagy, J. L. Fox, and T. E. Cravens (1998), Solar cycle variability of hot oxygen atoms at Mars, *J. Geophys. Res.*, *103*(A12), 29,339–29,342.

Kivelson, M. G., and C. T. Russell (1995), *Introduction to Space Physics*, Cambridge Univ. Press, Cambridge, U. K.

Kolesnikova, E., and C. Beghin (2001), Instability problem of the electric field antennas on the Polar spacecraft, *Radio Sci.*, *36*(2), 203–221.

Kolesnikova, E., C. Béghin, R. Grard, and C. Escoubet (2001), The electrical stability of the electric field antennas in the plasmasphere, *J. Atmos. Sol. Terr. Phys.*, *63*(11), 1217–1224.

Livesey, W., C. Kennel, and C. Russell (1982), ISEE-1 and -2 observations of magnetic field strength overshoots in quasi-perpendicular bow shocks, *Geophys. Res. Lett.*, *9*(9), 1037–1040.

Lundin, R., et al. (2006a), Plasma acceleration above Martian magnetic anomalies, *Science*, *311*(5763), 980–983.

Lundin, R., et al. (2006b), Ionospheric plasma acceleration at Mars: ASPERA-3 results, *Icarus*, *182*(2), 308–319.

Ma, Y., A. F. Nagy, I. V. Sokolov, and K. C. Hansen (2004), Three-dimensional, multispecies, high spatial resolution MHD studies of the solar wind interaction with Mars, *J. Geophys. Res.*, *109*, A07211, doi:10.1029/2003JA010367.

Malaspina, D. (2010), Microphysics of the solar wind, PhD thesis, Univ. of Colo., Boulder.

Matta, M., M. Galand, L. Moore, M. Mendillo, and P. Withers (2014), Numerical simulations of ion and electron temperatures in the ionosphere of Mars: Multiple ions and diurnal variations, *Icarus*, *227*, 78–88.

Mazelle, C., and F. M. Neubauer (1993), Discrete wave packets at the proton cyclotron frequency at comet P/Halley, *Geophys. Res. Lett.*, *20*(2), 153–156.

Mazelle, C., et al. (2004), Bow shock and upstream phenomena at Mars, in *Mars, Magnetism and Its Interaction With the Solar Wind*, edited by D. Winterhalter, M. Acuña and A. Zakharov, pp. 115–181, Springer, Netherlands.

Mellott, M., and W. Livesey (1987), Shock overshoots revisited, *J. Geophys. Res.*, *92*(A12), 13,661–13,665.

Moses, S., F. Coroniti, and F. Scarf (1988), Expectations for the microphysics of the Mars-solar wind interaction, *Geophys. Res. Lett.*, *15*(5), 429–432.

Papadopoulos, K. (1971), Ion thermalization in the Earth's bow shock, *J. Geophys. Res.*, *76*(16), 3806–3810.

Parker, E. N. (1963), *Interplanetary Dynamical Processes*, vol. 1, Interscience, New York.

Paschmann, G., N. Sckopke, I. Papamastorakis, J. Asbridge, S. Bame, and J. Gosling (1981), Characteristics of reflected and diffuse ions upstream from the Earth's bow shock, *J. Geophys. Res.*, *86*(A6), 4355–4364.

Romanelli, N., et al. (2016), Proton cyclotron waves occurrence rate upstream from Mars observed by MAVEN: Associated variability of the Martian upper atmosphere, *J. Geophys. Res. Space Physics*, *121*, 11,113–11,128, doi:10.1002/2016JA023270.

Rosenbauer, H., et al. (1989), Ions of Martian origin and plasma sheet in the Martian magnetosphere: Initial results of the TAUS experiment, *Nature*, *341*(6243), 612–614.

Ruhunusiri, S., J. Halekas, J. Connerney, J. Espley, J. McFadden, D. Larson, D. Mitchell, C. Mazelle, and B. Jakosky (2015), Low-frequency waves in the Martian magnetosphere and their response to upstream solar wind driving conditions, *Geophys. Res. Lett.*, *42*, 8917–8924, doi:10.1002/2015GL064968.

Russell, C., J. Luhmann, K. Schwingenschuh, W. Riedler, and Y. Yeroshenko (1990), Upstream waves at Mars: Phobos observations, *Geophys. Res. Lett.*, *17*(6), 897–900.

Sagdeev, R., V. Shapiro, V. Shevchenko, A. Zacharov, P. Kiraly, K. Szego, A. Nagy, and R. Grard (1990), Wave activity in the neighborhood of the bowshock of Mars, *Geophys. Res. Lett.*, *17*(6), 893–896.

Scarf, F., W. Taylor, C. Russell, and R. Elphic (1980), Pioneer Venus plasma wave observations: The solar wind-Venus interaction, *J. Geophys. Res.*, *85*(A13), 7599–7612.

Sckopke, N., G. Paschmann, A. Brinca, C. Carlson, and H. Lühr (1990), Ion thermalization in quasi-perpendicular shocks involving reflected ions, *J. Geophys. Res.*, *95*(A5), 6337–6352.

Shan, L., Q. Lu, M. Wu, X. Gao, C. Huang, T. Zhang, and S. Wang (2014), Transmission of large-amplitude ULF waves through a quasi-parallel shock at Venus, *J. Geophys. Res. Space Physics*, *119*, 237–245, doi:10.1002/2013JA019396.

Shapiro, V., K. Szegö, S. Ride, A. Nagy, and V. Shevchenko (1995), On the interaction between the shocked solar wind and the planetary ions on the dayside of Venus, *J. Geophys. Res.*, *100*(A11), 21,289–21,305.

Slavin, J., K. Schwingenschuh, W. Riedler, and Y. Yeroshenko (1991), The solar wind interaction with Mars: Mariner 4, MARS 2, MARS 3, MARS 5, and Phobos 2 observations of bow shock position and shape, *J. Geophys. Res.*, *96*(A7), 11,235–11,241.

Taylor, W., F. Scarf, C. Russell, and L. Brace (1979), Absorption of whistler mode waves in the ionosphere of Venus, *Science*, *205*(4401), 112–114.

Thomas, B. T., and E. J. Smith (1980), The Parker spiral configuration of the interplanetary magnetic field between 1 and 8.5 AU, *J. Geophys. Res.*, *85*(A12), 6861–6867.

Trotignon, J., C. Mazelle, C. Bertucci, and M. Acuna (2006), Martian shock and magnetic pile-up boundary positions and shapes determined from the Phobos 2 and Mars Global Surveyor data sets, *Planet. Space Sci.*, *54*(4), 357–369.

Trotignon, J. G., E. Dubinin, R. Grard, S. Barabash, and R. Lundin (1996), Martian planetopause as seen by the Plasma Wave System onboard Phobos 2, *J. Geophys. Res.*, *101*(A11), 24,965–24,977.

Valeille, A., M. R. Combi, S. W. Bougher, V. Tenishev, and A. F. Nagy (2009), Three-dimensional study of Mars upper thermosphere/ionosphere and hot oxygen corona: 2. Solar cycle, seasonal variations, and evolution over history, *J. Geophys. Res.*, *114*, E11006, doi:10.1029/2009JE003389.

Vignes, D., C. Mazelle, H. Rme, M. Acuna, J. Connerney, R. Lin, D. Mitchell, P. Cloutier, D. Crider, and N. Ness (2000), The solar wind interaction with Mars: Locations and shapes of the bow shock and the magnetic pile-up boundary from the observations of the MAG/ER Experiment onboard Mars Global Surveyor, *Geophys. Res. Lett.*, *27*(1), 49–52.